MASTER THESIS

A Space-Time Study of the Electron-Electron Interaction in High-T_C Parent Compound La_2CuO_4: In Search of an Attractive Effective Interaction

Tor Sjöstrand

Supervisors:
Ferdi Aryasetiawan & Fredrik Nilsson

DEPARTMENT OF PHYSICS
DIVISION OF MATHEMATICAL PHYSICS

LUND UNIVERSITY

2016

Abstract

The superconductivity under doping in the famous cuprate compounds is believed to originate in the CuO_2 planes. The mediator of pairing is generally accepted to be induced from electronic degrees of freedom. While many mechanisms, such as spin fluctuations, have been proposed throughout the years, little research has been carried out on the role of the retarded attraction due to electronic overscreening.

In this study, the dynamically screened interaction $W(\mathbf{r}, \mathbf{r}'; t)$ is studied in the CuO_2 planes of the parent compound La_2CuO_4. To this end, a repulsive test charge, representing an electron, is introduced at various $\mathbf{r}'$ in the CuO_2 plane, and $W(\mathbf{r}, \mathbf{r}'; t)$ is calculated as a function of $\mathbf{r}$ and t. The aim is to explore the possibility of the existence of an attractive effective interaction between electrons. The static screened interaction $W(\mathbf{r}, \mathbf{r}'; \omega = 0)$, which is the time average of $W(\mathbf{r}, \mathbf{r}'; t)$ is also studied. In addition, the effective interactions $U_1(\mathbf{r}, \mathbf{r}'; t)$ and $U_3(\mathbf{r}, \mathbf{r}'; t)$, corresponding to the well-known one- and three-band models, are investigated using the constrained random-phase approximation (cRPA). Substantial regions of the CuO_2 plane do indeed exhibit an attractive effective interaction, with both U_1 and U_3 being negative. On the other hand, the extent of such regions is significantly smaller in $SrVO_3$, a *non-superconducting* metal.

The present work suggests that future studies of electronic overscreening as a possible pairing mechanism is worth consideration. The same *ab initio* parameters as obtained and utilized in this work can be used to construct a Hubbard-Holstein model, within which the gap function can be calculated by solving the Eliashberg equations.

Acknowledgements

I would like to express my sincere gratitude to Professor Ferdi Aryasetiawan and Ph.D. Student Fredrik Nilsson, Lund University, for their passionate assistance and supervision throughout the course of this master thesis. I also would like to show my appreciation to Doctor Christoph Friedrich, Forschungszentrum Jülich, for providing valuable guidance on the computer codes and numerical implementation during his visit in Lund, and to Associate Professor Claudio Verdozzi, Lund University, for spending time on examining this study. Finally, I would like to dedicate this thesis to my beloved parents, Åsa and Per, and sister Linn, for always encouraging me to follow my dreams and for supporting me even on my busiest of days.

Abbreviations, Units and Symbols

Abbreviations

AF	Antiferromagnetic
ARPES	Angle-resolved photoemission spectroscopy
BCS	Bardeen-Cooper-Schrieffer
BZ	(Full) Brillouin zone
cRPA	Constrained random-phase approximation
DFT	Density functional theory
FLAPW	Full potential linearized augmented plane wave
GS	Ground state
GWA	GW approximation ($\Sigma = iGW$)
IBZ	Irreducible Brillouin zone
IR	Interstitial region
KS	Kohn-Sham
LDA	Local density approximation
LHB	Lower Hubbard band
LMTO	Linear muffin-tin orbital
MPB	Mixed product basis
MT	Muffin tin
PW	Polarization wave
RPA	Random-phase approximation
TDHA	Time-dependent Hartree approximation (= RPA)
UHB	Upper Hubbard band
xc	Exchange-Correlation
ZRS	Zhang-Rice singlet

System of Units

Atomic units:	$\hbar = 1$	Planck's reduced constant	$m_\mathrm{e} = 1$	Electron mass
	$e = 1$	Elementary charge	$\varepsilon_0 = 1/4\pi$	Permittivity of free space

Symbols

A	Spectral function
A^0	Non-interacting spectral function
α	Smearing factor in Ewald summation
$B^{\mathbf{k}}_{\alpha}$	Mixed product basis function
$\tilde{B}^{\mathbf{k}}_{\alpha}$	Biorthogonal mixed product basis function
$\hat{c}^{\sigma\dagger}_{n\mathbf{k}}/\hat{c}^{\sigma}_{n\mathbf{k}}$	Electron creation/annihilation operator (n: Band index. $\mathbf{k}$ and σ in this list)
$\hat{\gamma}^{\dagger}_{\mathbf{k}\sigma}/\hat{\gamma}_{\mathbf{k}\sigma}$	Quasi-particle creation/annihilation operator
Γ	Vertex function
D	Boson Green function
$\delta\rho$	Induced electron density
$\widetilde{\delta\rho}^{\mathrm{cRPA}}$	Induced electron density caused by screening channels in $\tilde{P}^{\mathrm{r0}}$
Δ	Superconducting gap function
Δ_{CT}	Charge transfer energy
ϵ^{-1}	Inverse dielectric function
$\varepsilon^{\sigma}_{n\mathbf{k}}$	Electron dispersion

E_F	Fermi energy
$E_{\mathbf{k}}$	Quasi-particle dispersion
E_{xc}	Exchange-correlation energy
G	Electron Green function
G^0	Non-interacting electron Green function
$\mathbf{G}$	Reciprocal lattice vector
$\mathbf{k}$	Crystal momentum
Λ	Electron-plasmon coupling
M	Mass operator
μ/μ_γ	Electron/Quasi-particle chemical potential
$\hat{n}^\sigma_{n\mathbf{k}}$	Electron number operator ($= \hat{c}^{\sigma\dagger}_{n\mathbf{k}}\hat{c}^\sigma_{n\mathbf{k}}$)
$N_{\mathbf{k}}$	Number of $\mathbf{k}$-mesh points
N_α	Number of mixed product basis functions
P	Polarization function
P^0	Non-interacting polarization function
P^{r0}	Non-interacting "high-energy" polarization in cRPA
$\tilde{P}^{\text{r0}}$	Non-interacting "high-energy" polarization in disentangled cRPA
$\mathcal{P}$	Subspace of $\tilde{P}^{\text{r0}}$
Π	Boson self-energy
R	Linear (electron) density responce function
R^{RPA}	Linear density responce function in RPA
$\tilde{R}^{\text{cRPA}}$	"High-energy" linear density responce function in disentangled cRPA
ρ	Ground-state electron density
σ	Electron spin ($\uparrow = +1/2$ or $\downarrow = -1/2$)
σ_1, σ_2, σ_3	Pauli matrices
Σ	Electron self-energy
t	Time *or* effective one-electron transfer ("hopping parameter")
T	Temperature
$\mathcal{T}$	Time-ordering operator
$\mathbf{T}$	Lattice vector
τ	Time-delay ($t - t'$)
T_C	Superconducting critical temperature
U	On-site repulsion ("Hubbard U")
U (U_1, U_3)	Partially screened interaction (effective interaction in 1- and 3-band model)
U^c	Correlated part of U ($U - v$)
U^r	Retarded partially screened interaction
U^{cr}	Correlated part of U^r ($U^r - v$)
v	Bare Coulomb interaction
V_{H}	Hartree potential
V_{xc}	Exchange-correlation potential
$\phi^\sigma_{n\mathbf{k}}$	Kohn-Sham eigenstates
φ	Time-dependent probing field
W	Fully screened interaction
W^c	Correlated part of W ($W - v$)
χ	Shift function
Y_{lm}	Spherical harmonic
Z	Renormalization factor
ω	Electron excitation energy
ω_n	Matsubara frequency
Ω	Unit cell volume *or* plasmon energy

Contents

Chapter 1

Introduction

Several compounds containing CuO_2 planes, called cuprates, become superconducting with a high critical temperature T_C when doped with electrons or holes. [1] The dream of achieving superconductivity at room temperature and the applications this would have in technology, such as lossless transmission of electricity, has led to great focus on these materials. The question arises: "What causes the pairing between electrons in the cuprates?" Several mechanisms have been proposed, many of electronic origin. Little attention has been paid on electronic overscreening, which could occur at different time-scales, and leads to an effective attraction between two electrons. The essential quantity, the effective electron-electron interaction U, naturally enters the Eliashberg equations of superconductivity (App. D:2), as shown in [2], which indicates that screening phenomena are essential in the pairing physics. The dynamics is hidden in the band structure, and extracted by a Wannier-interpolation procedure resulting in a few bands (as many as Wannier functions) close to the Fermi energy. For such a low-energy model, the dynamical effective interaction between electrons in these bands, U, gets screened by states outside the chosen subspace. [3]

The presence of overscreening in different band models will, due to the limited previous research, be the central topic of this work. But this requires U as a function of space, not as matrix elements in an incomplete localized basis constructed from the density functional theory (DFT) (App. A:1) eigenstates within local density approximation (LDA) (App. A:1), which is the usual way U is represented. The physics is also more transparent when studying U in time, not in frequency, as is normally done. The space and time dependence of U will therefore be extracted in this study in the CuO_2 planes of the prototypical cuprate parent compound La_2CuO_2, given a test charge (electron) also put in this plane. The main aim of providing this alternative perspective on the retarded electronic screening is to investigate the possibility of this constituting an important pairing mechanism. The pairing is generally believed to be confined to the CuO_2 planes [1]. So, if an attractive interaction can be found somewhere in these planes for a sufficiently long time, it is likely that electronic overscreening is important in the process of forming Cooper pairs. An effective *ab initio* model Hamiltonian (Hubbard-Holstein model [4]) can be constructed using the same interaction parameters as in this work, and the findings should indicate whether or not it is worthwhile to solve the Eliashberg equations for the superconducting gap within such a model.

The implementation is performed within the constrained random-phase approximation (cRPA), explained in section 2.3. cRPA is based on the assumption of weak vertex corrections (App. A:3) despite the fact that the Wannier-interpolated LDA-derived band crossing the Fermi energy (the antibonding combination of Cu $d_{x^2-y^2}$ and O p_x/p_y) is narrow and partially filled, and with main 3d character. At first, this may seem like a problem, not only

because of the partial filling, but also since the radial wave function of the 3d state is highly localized at the Cu sites, meaning that the mean-field assumption in LDA, based on that the electrons interacts with the average electron density in a finite region, fails. They instead interact very strongly merely with their closest neighbors. Adding an extra 3d electron on the same Cu site hence costs more energy than anticipated from LDA, due to the strong on-site repulsion between electrons, causing the band splitting needed to describe La_2CuO_4 as the insulator it actually is. The problem with the one-particle description lies in the local and energy-independent exchange-correlation potential V_{xc}, which should be generalized to a non-local end energy-dependent effective "potential", the self-energy Σ, to better take into account exchange and correlations. [5] However, in cRPA, the strong correlations do not enter the effective interaction U, as shown later, since the terms in the polarization function P (App. A:3) corresponding to transitions between two states contained within the low-energy subspace do not enter U. [3] This means that U can be obtained despite the assumption of weak vertex corrections.

The frequency-dependent U obtained within cRPA is a generalization of the on-site repulsion within the Hubbard-model (App. C), which is equal to the static value $U(\omega = 0)$. [3] The fully screened interaction W (App. A:3), which involves the strong correlations, will also be studied within cRPA. Hence, conclusions in this thesis regarding W will not be on as firm ground as for U. A "mixed product basis" derived from the LDA-eigenstates will be used to expand the linear density response function R, which uniquely determines U/W. These matrix elements are obtained from the GW code *SPEX* [6], a postprocessor of the DFT code *FLEUR* [7], based on the full potential linearized augumented plane wave (FLAPW) method. The spatial dependence of U/W will then be extracted by means of an Ewald summation procedure. The time-dependence is finally obtained by standard Fourier transformation. The induced electron density $\delta\rho$ will also be studied in space and time, making it easier to interpret W and U.

All necessary information needed to understand the results will be provided in "Theory and Motivation" and "Extraction of U in Space and Time". The former starts by presenting some general features of cuprate compounds, in particular La_2CuO_4. This follows by a motivation of why it is interesting to study the screened interaction in the cuprates, and further, as a function of space and time. "Theory and Motivation" ends by presenting cRPA, needed to understand the derivations following in "Extraction of U in Space and Time". To illustrate that the implementation seems to be successful, the first presented data in "Results and Discussion" are from studies of the static W in Nickel, where earlier studies have been performed in [8]. Comparisons are then made between the static W in La_2CuO_4 and $SrVO_3$, a non-superconducting metal. This is followed by a large amount of data of the static U in space as well as the dynamical U in space and time in La_2CuO_4, within the famous one- and three-band models. The report is then rounded off by "Summary and Conclusions" and "Future Directions".

Chapter 2

Theory and Motivation

2.1 Cuprates

It came as a great surprise when superconductivity was found in LaBaCuO at $30\,\mathrm{K}$ back in 1986, triggering research and synthesization of cuprate high-T_C superconductors, all with CuO_2 planes separated by charge reservoir layers and characterized by strong electron-electron correlations. These are antiferromagnetic insulators, but when doping the CuO_2 planes with electrons or holes, they become poor metals. When further reducing T they become superconducting with a characteristic high T_C [1], see Fig. 1. A discussion of conventional and unconventional superconductivity is given in App. D:1-2. The large correlations (on-site repulsions on the Cu site) and detailed phase-diagram call for a many-body description beyond BCS-theory. The knowledge of the cuprates is thereby mainly based on experimental data. The spectral function $A(\mathbf{k},\omega) = -(1/\pi)\mathrm{Im}\ G(\mathbf{k},\omega)$, for example, is obtained from angle-resolved photoemission spectroscopy (ARPES). G is the Green function (App. A:2). In terms of the self-energy Σ (App. A:2), G and A are given by [1]

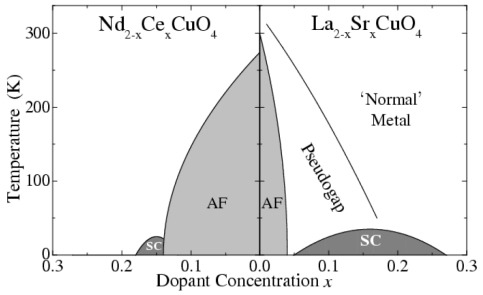

Figure 2.1: Typical phase diagram of hole- and electron-doped high-T_C superconductors (from [1]). AF: Antiferromagnet, SC: Superconductor. Pseudogap refers to an energy gap with critical temperature $> T_C$ in the normal state, present at the majority of the Fermi surface. [1]

$$G(\mathbf{k},\omega) = \frac{1}{\omega - \varepsilon(\mathbf{k}) - \Sigma(\mathbf{k},\omega)}$$

$$A(\mathbf{k},\omega) = -\frac{1}{\pi}\frac{\mathrm{Im}\ \Sigma(\mathbf{k},\omega)}{[\omega - \varepsilon(\mathbf{k}) - \mathrm{Re}\ \Sigma(\mathbf{k},\omega)]^2 + [\mathrm{Im}\ \Sigma(\mathbf{k},\omega)]^2}.$$

Im $G(\mathbf{k},\omega)$ and Re $G(\mathbf{k},\omega)$ are related through Kramers-Kronig relations to fulfil causality, meaning that $\Sigma(\mathbf{k},\omega)$ can be calculated, which contains all the correlation effects. [1] ARPES has, for reasons like this, proved to be extremely important for the study of the cuprates.

In this thesis, only one prototypical cuprate, $La_{2-x}Sr_xCuO_4$, will be studied, with a tetragonal crystal structure at high T. It has been shown that even at low T, the properties are captured assuming the same symmetry. [1] The crystal structure and LDA band structure, obtained using *FLEUR*, of the parent compound La_2CuO_4 is shown in Fig. 2.2, together with that of $SrVO_3$, a non-superconducting metal which later in this study will be compared with La_2CuO_4. In La_2CuO_4 the CuO_2 planes are separated by two LaO planes, and in the doped system some La atoms are replaced by Sr which induces holes into the CuO_2 planes. The La,

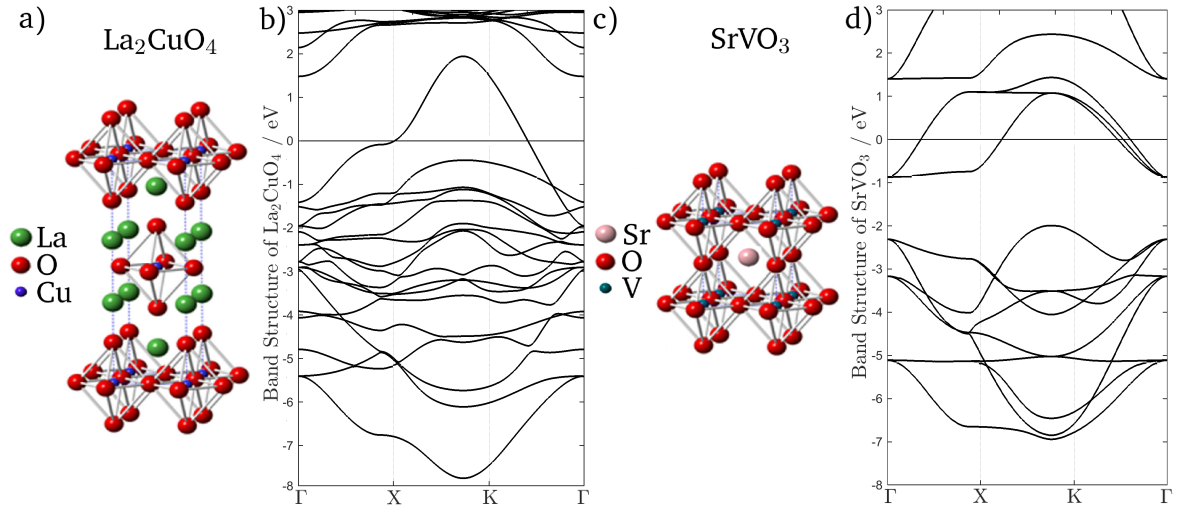

Figure 2.2: a) Crystal structure of La_2CuO_4 (from [9] but modified). b) LDA band structure of La_2CuO_4. c) Crystal structure of $SrVO_3$. d) LDA band structure of $SrVO_3$. $\Gamma = (0,0,0)$, $X = (\pi,0,0)$, $K = (\pi,\pi,0)$.

Sr and O atoms between the CuO_2 planes are said to comprise a charge reservoir layer. $La_{2-x}Sr_xCuO_4$, which only has one CuO_2 plane per unit cell, is categorized as a *single-layer* cuprate. The simple structure does not make it less archetypical of cuprates compounds, rather the opposite. The superconducting properties in $La_{2-x}Sr_xCuO_4$ are, like in other cuprates, thought to be confined to the CuO_2 planes since the low-energy LDA bands (close to E_F) are of main Cu $3d_{x^2-y^2}$ and O $2p_x/p_y$ character, thus determining the macroscopic properties. At zero doping, band structure and mean-field models predict a paramagnetic metal due to the half-filled narrow d band (Fig. 2.2 b)), but it is an antiferromagnetic (AF) insulator [1], reflecting the strong electron correlations.

A popular method to introduce many-body corrections necessary to explain this discrepancy and other properties is the Hubbard model (App. C). The main quantity U, the on-site repulsion, is often treated as a material-dependent adjustable parameter. A realistic model can however be obtained if U (and possible additional parameters) is obtained by *ab initio* methods. The constrained random-phase approximation (cRPA), which will be explained later, allows the calculation of U from first-principles and also introduces frequency-dependence into U. This frequency-dependence naturally enters when integrating out high-energy states from the original Hamiltonian, and the so called partially screened interaction $U(\omega)$ is the effective bare interaction in the resulting subspace. [10] It was found recently that a frequency-dependent interaction is needed to describe the undoped parent compound La_2CuO_4 as an insulator with a gap in the spectral function. [11] Further, the AF nature is understood directly from the Hubbard model in which electrons due to the large U are localized, but if electrons at neighbouring sites have opposite spin they can hop back and forth making antiparallel spin energetically favourable.

2.2 Why Study the Screened Interaction of La_2CuO_4 in Space and Time?

There are quite a few reasons to study the fully and partially screened interaction, $W(\mathbf{r},\mathbf{r}';\tau)$ and $U(\mathbf{r},\mathbf{r}';\tau)$, in space and time of the parent compound La_2CuO_4. Three reasons will be discussed, where (i) and (ii) relate to the screened interaction itself, and (iii) to the space-time extraction.

(i) U Relates to Superconductivity

The screened interaction has been shown to be intimately related to superconductivity within the Hubbard model. It is therefore worth spending the first part of this section on explaining this model and its general results for the cuprates, and then discussing superconductivity.

Consider a single CuO_2 layer and neglect the small interlayer hopping. The main physics is captured by only considering a few bands close to E_F by means of a downfolding procedure (see section 2.3). A common downfolding is to a 3-band model with the antibonding and bonding combination of the Cu $3d_{x^2-y^2}$ and O $2p_\sigma$ bands ($\sigma = x$ or y) and a non-bonding p-orbital. Further downfolding to one band, where only the antibonding combination (with dominating $d_{x^2-y^2}$-component) at the Fermi energy is included, results in nominal Cu sites connected by an effective one-electron transfer t and on-site repulsion U, represented by the one-band Hubbard model [12], with Hamiltonian [3] (App. C for details)

$$\hat{H} = t \sum_{\sigma\langle ij\rangle\subset \mathrm{d}} \hat{c}^\dagger_{i\sigma}\hat{c}_{j\sigma} + U \sum_{i\subset \mathrm{d}} \hat{n}_{i\uparrow}\hat{n}_{i\downarrow}.$$

La_2CuO_4 has one d-hole resulting in a half-filled $d_{x^2-y^2}$-band of spin $1/2$. The minimum charge excitation energy is not the on-site repulsion U, but the charge transfer energy Δ_{CT} between Cu and O due to hybridization of Cu $3d_{x^2-y^2}$ and O $2p_\sigma$. [13] The large U is the reason for the failure of the LDA band structure and splits Cu $3d_{x^2-y^2}$ into an upper and lower "Hubbard band" (UHB and LHB) within the 3-band model, see Fig. 2.3a)-b). When adding an O $2p_\sigma$ hole of opposite spin to the Cu $3d_{x^2-y^2}$ hole the lowest energy state is a local "Zhang-Rice singlet"' (ZRS), in which the O $2p_\sigma$ hole surrounds the Cu site. One thus interprets ZRS as a LHB within the 1-band model (Fig. 2.3c)-d)), split from the band of $d_{x^2-y^2}$-symmetry by the effective Coulomb repulsion $U_{\mathrm{gap}} = \Delta_{\mathrm{CT}}$. [13] The static one-band model ignores the charge transfer insulator property of the cuprates, but has been used to show (in [12]) that with hole doping, so that $\langle \hat{n}_{i\uparrow} + \hat{n}_{i\downarrow}\rangle < 1$, U can give rise to Cooper pairing within the $d_{x^2-y^2}$-state, which avoids spatial regions where the static effective interaction is repulsive. Just like two electrons that correlate in time to avoid the short-time Coulomb repulsion ($v\delta(t-t')$) in the case of electron-phonon interaction, two electrons in the $d_{x^2-y^2}$-orbit avoid the irreducible singlet electron-electron interaction. Quantum Monte Carlo-simulations and experiments also show that the long-range antiferromagnetic order disappears at non-zero doping. [12]

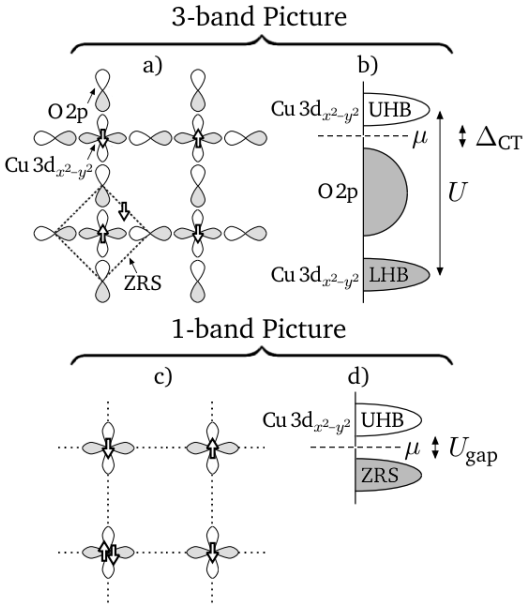

Figure 2.3: Orbitals involved in a 3-band model (a) and 1-band model (c) and schematic density of states in a 3-band model (b) and 1-band model (d). (from [13] but modified)

The static Hubbard model cannot explain superconductivity perfectly, but the screened interaction enters naturally into the *Eliashberg equations* (App. D:2). For simple metals, electrons may (in a single-band picture) be separated into two classes. 1) *Valence electrons*: Resembling a homogeneous interacting Fermi liquid, which may form Cooper pairs when screened, due to Friedel oscillations with regions of attraction (*intrinsic superconductivity*). 2) *Core-electrons*: Quasi-localized and stable against Cooper pairing, adding to the polarizability of

the ionic system. [2] In analogy to this separation done for simple metals, in the cuprates Cu 3d make up valence electrons and O 2p play the role of the core electrons. Assuming 1) and 2) have non-overlapping bands, the dynamics of 1) is described by the plasmons and of 2) by the quantized polarization waves (PW). The PW do, to first order, capture the freedom of the core electrons to move relative to their nuclei. The PW are thus of dipole character, and the phonons (following the nuclei) of monopole character in the relative position of the core electrons. This multipole expansion assumes small overlaps between core-electrons in different ions. The PW can overscreen an external electron, which thus attracts another, and in metallic systems the valence electrons also screen the PW. The explicit form of the effective valence electron-electron interaction U will not be given here, but may be found in [2]. U contains the effects of correlation hole charge fluctuations, spin fluctuations and screened polarization waves which couple to the former two. These electronic pairing channels do not fulfil Migdal's theorem (App. D:2), requiring a strong-coupling picture when determining the gap function $\Delta(\mathbf{k}, i\omega_n)$. The l-wave Eliashberg equation reads (at T just below T_C)

$$\Delta_l(\mathbf{k}, i\omega_n) = \tag{2.1}$$
$$-\frac{T}{2}\sum_{\omega_{n'}}\sum_{\mathbf{k}'}|G(\mathbf{k}', i\omega_{n'})|^2\int_0^\pi d\theta \sin\theta P_l(\cos\theta)U(\mathbf{k}-\mathbf{k}', i\omega_n - i\omega_{n'})\Delta_l(\mathbf{k}', i\omega_{n'})$$

where $\cos\theta = (\mathbf{k}\cdot\mathbf{k}')/(kk')$, and P_l are Legendre polynomials. The imaginary-axis formulation[†] has been used in 2.1 (and App. D:2). The inclusion of polarization waves increases T_C significantly, both for s-wave and d-wave pairing, [2] but the main point of this section is that U enters naturally in the gap equation 2.1.

[†]"Imaginary-axis" refers to that in this formulation operators evolve non-unitarily, like if time $t = it'$ is imaginary (t' real). This is useful for finite T calculations, where the retarded G is difficult to get by many-body perturbation theory. The imaginary-axis G is 2β-periodic ($\beta = 1/T$) for $t' \in [-\beta, \beta]$, allowing for Fourier expansion, with non-zero components for the "Matsubara frequencies" $i\omega_n$ (see App. D:2). The retarded G is found by analytical continuation $i\omega_n \to \omega + i\eta$, where η is real and infinitesimal. [14]

(ii) RPA is Valid for U

In La_2CuO_4, most of the correlations are confined to a single LDA band of dominating Cu $d_{x^2-y^2}$ character at the Fermi energy. This allows for a one-band downfolding, explained in section 2.3, where this band makes up the low-energy subspace and the partially screened interaction U_1 (the effective bare interaction) takes into account all screening channels except within this subspace. A considerable amount of screening is then caused by the O 2p states, which are close to the Fermi energy. In the three-band downfolding, these are also captured to a large extent within the low-energy subspace, with effective interaction U_3. This separation of electrons into a low- and high-energy subspace is very similar to the separation in point (i). Since the strong correlations never enter U_1 and U_3, the random-phase approximation (RPA) (App. B) is most likely sufficient, where the interacting polarization P is replaced by the non-interacting polarization P^0. This will be explained in section 2.3. If this was not the case a precise implementation would be, if not impossible, much more demanding. W does however contain the strongly correlated low-energy screening, and the RPA treatment can be questioned. Nonetheless, to its favour points the LDA Fermi surface of many cuprates ($YBa_2Cu_3O_7$ in [15]) which closely resembles measurements. There is thus a good reason to believe that low-energy excitations are well captured within RPA.

(iii) A Space-Time Picture of the Screening is Revealing

In space, the screened interaction U is usually associated with a simplified Yukawa potential $e^{-\lambda r}/r$, although the information for a spatial extraction is accessible. Instead, U is normally calculated as matrix elements in an incomplete localized basis derived from the LDA eigenstates, obtained as a function of frequency. Physical insights may have been overlooked due to this tradition. A space-time picture should provide knowledge of regions of attractive interaction and the time scales of such an attraction, which may be valuable for investigating the possibility of pair formation. Further, by comparing the partially screened interaction within 1- and 3-band downfoldings, the p-d screening can be approximately isolated, meaning that the orbital dynamics of particular screening channels can be studied in space and time. The p-d channel is already known to be characterized by a sharp 9 eV excitation localized at the Cu sites [11], and a temporal oscillation of this frequency can be anticipated. The partially screened interactions U_1 and U_3 can also be compared with the fully screened interaction W, keeping in mind the possible limitation of RPA for the latter.

2.3 Constrained Random-Phase Approximation

By downfolding a many-particle problem onto a low-energy subspace (d subspace) a frequency-dependence is introduced into the Hubbard U within the Green function formalism. The Dirac field operator can be split into a low-energy d-part and a high-energy r-part [16] (r for "rest" subspace):

$$\hat{\psi}_D(\mathbf{r}) = \hat{\psi}_{\mathrm{d}}(\mathbf{r}) + \hat{\psi}_{\mathrm{r}}(\mathbf{r}) = \sum_{i\subset \mathrm{d}} \phi_i(\mathbf{r})\hat{c}_i + \sum_{i\subset \mathrm{r}} \phi_i(\mathbf{r})\hat{c}_i$$

where $\{|\phi_i\rangle\}$ are usually Kohn-Sham states and $\{\hat{c}_i\}$ annihilation operators. Introducing a time-dependent probing field $\varphi(\mathbf{r},t)$ leads to a Green function G^{d} connecting states within d and another G^{rd} connecting d and r. The Hedin equations (App. A:3) are downfolded to the d subspace. The selfenergy $\Sigma = \Sigma^{\mathrm{d}} + \Sigma^{\mathrm{rd}} + \Sigma^{\mathrm{drd}}$, is no simple projection on the low-energy subspace d since this couples to the high-energy subspace r through the latter two terms. The last term, the d-r hybridization, describes hopping d→r→d. When neglecting self-energy effects from the r subspace, Σ^{rd} and Σ^{drd}, the downfolded Hedin equations can be reduced to the Hubbard model, where $U(\omega = 0)$ is the "Hubbard U". [16] The polarization is further separated into

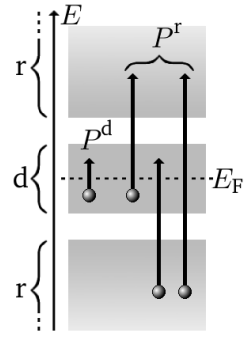

Figure 2.4: Schematic illustration of transitions related to P^{d} and P^{r}.

$$P = P^{\mathrm{d}} + P^{\mathrm{r}}.$$

P^{d} connects two d-states and P^{r} the rest, that is to say d-r and r-r as shown in Fig. 2.4. Using the relations (ϵ^{-1} and R are defined in App. A:3)

$$W = \epsilon^{-1} v \ , \ \epsilon^{-1} = 1 + vR \ , \ \epsilon = 1 - vP$$

and defining $W^{\mathrm{r}} = [1 - vP^{\mathrm{r}}]^{-1}v = (\epsilon^{\mathrm{r}})^{-1}v$ yields [3]

$$W = W^{\mathrm{r}} + W^{\mathrm{r}}P^{\mathrm{d}}W.$$

The similarity with $W = v + vPW$ allows W^{r} to be interpreted as the effective interaction within d, since further screening by P^{d} yields W. The Hubbard U thus generalizes to

$$U(\mathbf{r},\mathbf{r}';\omega) = W^{\mathrm{r}}(\mathbf{r},\mathbf{r}';\omega). \tag{2.2}$$

Since $U = W^{\mathrm{r}} = (\epsilon^{\mathrm{r}})^{-1}v$ is determined only by $P^{\mathrm{r}} = P - P^{\mathrm{d}}$, and r, with its extended states, is weakly correlated, RPA can be applied to P^{r}. This is called *constrained* RPA or cRPA. P^{r} is

thus replaced by the non-interacting P^{r0} (App. B):

$$P^{\mathrm{r0}}(\mathbf{r},\mathbf{r}';\omega) = \sum_{\sigma} \sum_{\mathbf{k},\mathbf{k}'\in \mathrm{BZ}} \left(\sum_{n}^{\mathrm{occ}} \sum_{n'}^{\mathrm{unocc}} P^{0,\sigma}_{n\mathbf{k},n'\mathbf{k}'}(\mathbf{r},\mathbf{r}';\omega) - \sum_{n\in \mathrm{d}}^{\mathrm{occ}} \sum_{n'\in \mathrm{d}}^{\mathrm{unocc}} P^{0,\sigma}_{n\mathbf{k},n'\mathbf{k}'}(\mathbf{r},\mathbf{r}';\omega) \right)$$

$$P^{0,\sigma}_{n\mathbf{k},n'\mathbf{k}'}(\mathbf{r},\mathbf{r}';\omega) = \phi^{\sigma *}_{n\mathbf{k}}(\mathbf{r})\phi^{\sigma}_{n'\mathbf{k}'}(\mathbf{r})\phi^{\sigma}_{n\mathbf{k}}(\mathbf{r}')\phi^{\sigma *}_{n'\mathbf{k}'}(\mathbf{r}') \times \left(\frac{1}{\omega + \varepsilon^{\sigma}_{n\mathbf{k}} - \varepsilon^{\sigma}_{n'\mathbf{k}'} + i0^{+}} - \frac{1}{\omega - \varepsilon^{\sigma}_{n\mathbf{k}} + \varepsilon^{\sigma}_{n'\mathbf{k}'} - i0^{+}} \right).$$

The eigenvalues and -states of the mean-field Hamiltonian, $\{|\phi^{\sigma}_{n\mathbf{k}}\rangle\}$ and $\{\varepsilon^{\sigma}_{n\mathbf{k}}\}$, are usually taken as Kohn-Sham eigenstates from a self-consistent DFT-calculation. U is more long-ranged than W since it does not contain low-energy "metallic" transitions. [3] In the following, i will be used to denote the combined labels $n\mathbf{k}$.

In La_2CuO_4, the bands in d are entangled with bands in r and cRPA needs to be modified to isolate the subspaces. One way is to choose d as a set of localized Wannier orbitals obtained from the Kohn-Sham eigenstates within an energy-window, and diagonalize the Hamiltonian in this subspace, yielding eigenstates $\{|\tilde{\phi}_i\rangle\}$ and -energies $\{\tilde{\varepsilon}_i\}$. After checking that the band structure close to E_F is reproduced, $\tilde{P}^{\mathrm{d0}}$ is defined as P^{d0} but using $\{|\tilde{\phi}_i\rangle\}$ and $\{\tilde{\varepsilon}_i\}$. With $\hat{\mathcal{P}} = \sum_{i=1}^{N_d} |\tilde{\phi}_i\rangle\langle\tilde{\phi}_i|$ being the d projection operator, r is defined by $\{|\chi_i\rangle\} = (1 - \hat{\mathcal{P}})\{|\phi_i\rangle\}$, which is orthogonal to d, yielding disentangled d- and r-bands (close to the original) with zero H_{dr} and H_{rd}. By constructing $\tilde{P}^{0}$, the disentangled non-interacting polarization, $\tilde{P}^{\mathrm{r0}}$ is defined as $\tilde{P}^{0} - \tilde{P}^{\mathrm{d0}}$. [3] $\tilde{P}^{\mathrm{r0}}$ is thus used instead of P^{r0} for the calculation of U in the case of disentangled bands. The disentangled Wannier interpolated band structures within the 1- and 3-band models are presented in Fig. 3.1, obtained using *SPEX*. The different band models yield different effective dynamical interactions $U(\omega)$.

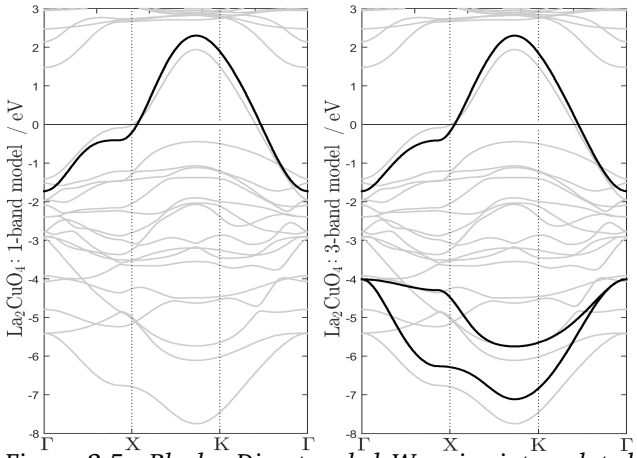

Figure 2.5: Black: Disentangled Wannier interpolated bands of La_2CuO_4 in a 1- (left) and 3-band model (right). Grey: LDA band structure. $\Gamma = (0,0,0)$, $X = (\pi,0,0)$, $K = (\pi,\pi,0)$.

The 1-band model in section 2.2(i), based on Wannier functions, has been shown in [11] to yield a sharp plasmon-like excitation in the imaginary-part of U_1 around $9\,\mathrm{eV}$. This excitation was further shown in [11] to be localized at the Cu sites and to have $\mathrm{d}_{x^2-y^2}$ character. Since this is not present in U_3 within a 3-band model it must come from transitions between the occupied bands of main O p character to the unoccupied part of the antibonding band of main Cu d character. The real-part of the Cu d-Cu d (Wannier) matrix element of U_1 was further shown to become negative in the vicinity of the $9\,\mathrm{eV}$ peak. W contains an additional peak at around $3\,\mathrm{eV}$ which is also localized at Cu, corresponding to transitions within the antibonding band. [11]

Chapter 3

Extraction of U in Space and Time

The extraction of $W(\mathbf{r},\mathbf{r}';\tau)$ is preceded by the calculation of matrix elements of the responce function $\{R^{\text{RPA}}(\mathbf{k},\omega)\}$ within RPA and the extraction of $U_1(\mathbf{r},\mathbf{r}';\tau)$ and $U_3(\mathbf{r},\mathbf{r}';\tau)$ by the calculation of $\{\tilde{R}^{\text{cRPA}}(\mathbf{k},\omega)\}$ within disentangled cRPA. Here (see App. B),

$$R^{\text{RPA}} = P^0 + P^0 v R^{\text{RPA}}$$
$$\tilde{R}^{\text{cRPA}} = \tilde{P}^{\text{r0}} + \tilde{P}^{\text{r0}} v \tilde{R}^{\text{cRPA}}.$$

These matrix elements are obtained using *customized SPEX* [17], a modified version of the GW code *SPEX* [6], which utilizes many-body perturbation theory for one-shot and self-consistent calculations of quasiparticle properties. The *customized* and original *SPEX* are postprocessors of the DFT code *FLEUR* [7], based on the full potential linearized augumented plane wave (FLAPW) method (used for calculating ground-state and excited-state properties of solids). *SPEX* takes as inputs LDA eigen-states and -energies from *FLEUR* obtained from a self-consistent DFT cycle. *Customized SPEX* has the additional feature of calculating maximally localized Wannier functions, allowing for disentangled cRPA and calculation of $\{\tilde{R}^{\text{cRPA}}(\mathbf{k},\omega)\}$.

While obtaining $\{\tilde{R}^{\text{cRPA}}(\mathbf{k},\omega)\}$ requires no code writing, the steps connected to the space-time extraction do. The flowchart in Fig. 3.1 summarizes the procedure, where the blue box contains the parts of the implementation where *customized SPEX* and *FLEUR* were used, and the green box the parts where additional code was written specifically for the space-time extraction. From here on, U will be used to label both W, U_1 and U_3 since the forms of all equations for U_1 and U_3 within disentangled cRPA are the same as for W within RPA (App. B) but with P^0/R^{RPA} replaced by $\tilde{P}^{\text{r0}}/\tilde{R}^{\text{cRPA}}$. On matrix form,

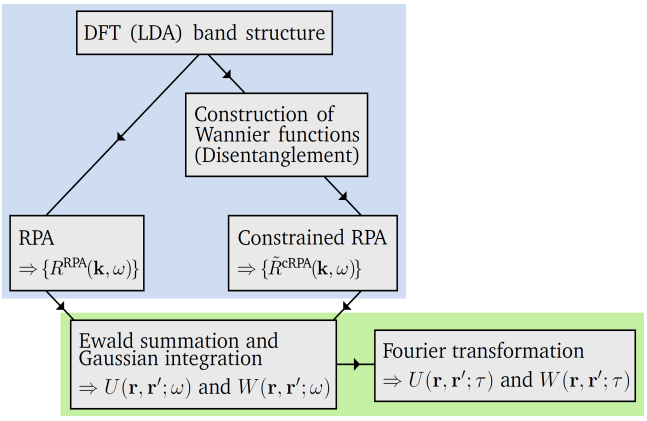

Figure 3.1: Steps to obtain $W(\mathbf{r},\mathbf{r}';\tau)$ and $U(\mathbf{r},\mathbf{r}';\tau)$. Blue box: Code exists (FLEUR and customized SPEX). Green box: Extensions of the existing code have been developed in this work.

$$U = v + U^c = v + v\tilde{P}^{\text{r0}}U = v + v\tilde{R}^{\text{cRPA}}v.$$

Note that the unknown spatial dependence in $U(\mathbf{r},\mathbf{r}';\omega)$ is entirely due to the correlation term $U^c(\mathbf{r},\mathbf{r}';\omega)$ since $v(|\mathbf{r}-\mathbf{r}'|) = 1/|\mathbf{r}-\mathbf{r}'|$ is known.

3.1 Mixed Product Basis

To obtain U in space and time the polarization $\tilde{P}^{\mathrm{r0}}$ must first be expressed in a basis which is complete in the subspace $\mathcal{P}$ of the polarization $\tilde{P}^{\mathrm{r0}}$. In *SPEX*, $\tilde{P}^{\mathrm{r0}}$ is given in a "mixed product basis" (MPB) obtained from the FLAPW basis. In the FLAPW method space is divided into spherical *muffin tins* MT(a) centered at atom a, and an *interstitial region*, IR$= \bigcap_{a=1}^{N_a} \mathrm{MT}(a)^{\complement}$. The basis functions read

$$\phi^{\sigma}_{n\mathbf{k}}(\mathbf{r}) = \begin{cases} \frac{1}{\sqrt{N}} \sum_{l=0}^{l_{\max}} \sum_{m=-l}^{l} \sum_{p=0}^{1} A^{n\mathbf{k}\sigma}_{almp} u^{\sigma}_{almp}(\mathbf{r}-\mathbf{R}_a) & , \quad \mathbf{r} \in \mathrm{MT}(a) \\ \frac{1}{\sqrt{V}} \sum_{|\mathbf{k}+\mathbf{G}|\leq G_{\max}} c^{n\mathbf{k}\sigma}_{\mathbf{G}} \mathrm{e}^{i(\mathbf{k}+\mathbf{G})\cdot\mathbf{r}} & , \quad \mathbf{r} \in \mathrm{IR}. \end{cases}$$

V is the crystal volume, N the number of unit cells, u^{σ}_{alm0} the KS solutions of the spherically averaged effective potential and $u^{\sigma}_{alm1} = \partial u^{\sigma}_{alm0}/\partial E^{\sigma}_{al}$ its energy-derivatives. The core states are obtained by solving the Dirac equation. $A^{n\mathbf{k}\sigma}_{almp}$ and $c^{n\mathbf{k}\sigma}_{\mathbf{G}}$ ensure continuity up to first derivative. [18]

A basis in the $\mathcal{P}$ subspace is obtained from products of FLAPW functions, but it is more useful to construct non-overlapping product functions, one set defined in the MT spheres, and the other in the IR. In MT(a), instead of $u^{\sigma *}_{almp}(\mathbf{r}) u^{\sigma}_{al'm'p'}(\mathbf{r})$ with angular part $Y^{*}_{lm}(\hat{\mathbf{r}}) Y_{l'm'}(\hat{\mathbf{r}})$ all $Y_{LM}(\hat{\mathbf{r}})$ with $|l-l'| \leq L \leq l+l'$ and $-L \leq M \leq L$ are used together with a radial part $U^{\sigma}_{aLP}(r) = u^{\sigma}_{alp}(r) u^{\sigma}_{al'p'}(r)$. P tracks all $\{l, l', p, p'\}$-combinations. The U^{σ}_{aLP}'s are not orthonormal, so the overlap matrix is diagonalized and only eigenvectors with eigenvalues above a threshold are kept. Summing over spin yields a spin-independent radial MT-basis $B_{aLP}(r)$. From $B_{aLP}(r) Y_{LM}(\hat{\mathbf{r}})$ Bloch functions $B^{\mathbf{k}}_{aLP}(\mathbf{r})$ are constructed which are only non-zero when $\mathbf{r} \in$ MT(a) up to arbitrary lattice translations. The IR plane wave products, are instead only non-zero when $\mathbf{r} \in$ IR up to lattice translations, and given by $B^{\mathbf{k}}_{\mathbf{G}}(\mathbf{r}) = \Omega^{-1/2} \mathrm{e}^{i(\mathbf{k}+\mathbf{G})\cdot\mathbf{r}}$, where Ω is the unit cell volume. The MPB is the combined set of spatially separated basis functions $\{B^{\mathbf{k}}_{\alpha}\} = \{B^{\mathbf{k}}_{aLMP}, B^{\mathbf{k}}_{\mathbf{G}}\}$, and is associated with a biorthogonal set $\{\tilde{B}^{\mathbf{k}}_{\alpha}\}$ fulfilling $\langle B^{\mathbf{k}}_{\alpha} | \tilde{B}^{\mathbf{k}}_{\beta} \rangle = \langle \tilde{B}^{\mathbf{k}}_{\alpha} | B^{\mathbf{k}}_{\beta} \rangle = \delta_{\alpha\beta}$ and $\sum_{\alpha} |B^{\mathbf{k}}_{\alpha}\rangle\langle \tilde{B}^{\mathbf{k}}_{\beta}| = \sum_{\alpha} |\tilde{B}^{\mathbf{k}}_{\alpha}\rangle\langle B^{\mathbf{k}}_{\beta}| = \mathbf{1}$ in $\mathcal{P}$. [18] In *SPEX* all MPB functions are given on a $\mathbf{k}$-mesh, a $4 \times 4 \times 4$-mesh in this work.

3.2 $U(\mathbf{r}, \mathbf{r}'; \omega)$ as a Basis Expansion

Given $U^{c}_{\alpha\beta}(\mathbf{k}; \omega) = \langle \tilde{B}^{\mathbf{k}}_{\alpha} | \hat{U^{c}}(\omega) | \tilde{B}^{\mathbf{k}}_{\beta} \rangle$ in the MPB a naïve approach to obtain $U(\mathbf{r}, \mathbf{r}'; \omega)$ is by a simple expansion of U^{c}:

$$U^{c}(\mathbf{r}, \mathbf{r}'; \omega) = \sum_{\mathbf{k} \in \mathrm{BZ}} w_{\mathbf{k}} \sum_{\alpha\beta} B^{\mathbf{k}}_{\alpha}(\mathbf{r}) U^{c}_{\alpha\beta}(\mathbf{k}; \omega) B^{\mathbf{k}*}_{\beta}(\mathbf{r}')$$

where $w_{\mathbf{k}\neq\Gamma} = 1/N_{\mathbf{k}}$ and the Γ-point requires special treatment. $N_{\mathbf{k}}$ is the number of $\mathbf{k}$-mesh points. Recall that $\{|B^{\mathbf{k}}_{\alpha}\rangle\}$ spans $\mathcal{P}$ since constructed from wavefunction products. Unfortunately, the product basis is not sufficient to calculate $U^{c}(\mathbf{r}, \mathbf{r}'; \omega)$, for which the full Hilbert space is required.

3.3 $U(\mathbf{r}, \mathbf{r}'; \omega)$ as an Interaction Expansion

That $\{|B^{\mathbf{k}}_{\alpha}\rangle\}$ is restricted to $\mathcal{P}$ can be used in a clever way by recognising that the linear density response function $\tilde{R}^{\mathrm{cRPA}}$ is also confined to $\mathcal{P}$. This is seen when expanding $\tilde{R}^{\mathrm{cRPA}}$ in $\tilde{P}^{\mathrm{r0}}$, which on matrix form reads $\tilde{R}^{\mathrm{cRPA}} = \tilde{P}^{\mathrm{r0}} + \tilde{P}^{\mathrm{r0}} v \tilde{P}^{\mathrm{r0}} + \ldots$. $\{|B^{\mathbf{k}}_{\alpha}\rangle\}$ is thus a complete basis

for $\tilde{R}^{\text{cRPA}}$, and the matrix elements can be obtained in the *SPEX*-code. Once $\tilde{R}^{\text{cRPA}}$ is known U^c can be obtained, which is the main idea of this method. U^c in terms of $\tilde{R}^{\text{cRPA}}$ reads

$$\begin{aligned} U^c(\mathbf{r},\mathbf{r}';\omega) &= \int d^3r_1 d^3r_2 v(|\mathbf{r}-\mathbf{r}_1|)\tilde{R}^{\text{cRPA}}(\mathbf{r}_1,\mathbf{r}_2;\omega)v(|\mathbf{r}_2-\mathbf{r}'|) \\ &= \int d^3r_1 v(|\mathbf{r}-\mathbf{r}_1|)\widetilde{\delta\rho}^{\text{cRPA}}(\mathbf{r}_1,\mathbf{r}';\omega). \end{aligned}$$

$\widetilde{\delta\rho}^{\text{cRPA}}(\mathbf{r}_1,\mathbf{r}';\omega)$ is the induced electron density at $\mathbf{r}_1$ caused by the screening channels in $\tilde{P}^{\text{r0}}$ due to a point charge at $\mathbf{r}'$ with potential $v(|\mathbf{r}_2-\mathbf{r}'|)$. The MPB matrix elements $\tilde{R}^{\text{cRPA}}_{\alpha\beta}(\mathbf{k};\omega) = \langle \tilde{B}^{\mathbf{k}}_\alpha | \widehat{\tilde{R}^{\text{cRPA}}}(\omega) | \tilde{B}^{\mathbf{k}}_\beta \rangle$ from *SPEX* allow for an "interaction expansion" of U^c:

$$U^c(\mathbf{r},\mathbf{r}';\omega) = \sum_{\mathbf{k}\in\text{BZ}} w_{\mathbf{k}} \sum_{\alpha\beta} \mathcal{I}^{\mathbf{k}}_\alpha(\mathbf{r})\tilde{R}^{\text{cRPA}}_{\alpha\beta}(\mathbf{k};\omega)\mathcal{I}^{\mathbf{k}*}_\beta(\mathbf{r}') \tag{3.1}$$

$$\mathcal{I}^{\mathbf{k}}_\alpha(\mathbf{r}) = \int d^3r_1 v(|\mathbf{r}-\mathbf{r}_1|)B^{\mathbf{k}}_\alpha(\mathbf{r}_1). \tag{3.2}$$

$w_{\mathbf{k}\neq\Gamma} = 1/N_{\mathbf{k}}$ and the Γ-point will be discussed in section 2.4.4. Note that the problem of projecting on $\mathcal{P}$ in section 2.4.2 has disappeared, the "interactions" $\{\mathcal{I}^{\mathbf{k}}_\alpha\}$ are not restricted to $\mathcal{P}$ as $\{B^{\mathbf{k}}_\alpha\}$ are. So, given $\{\tilde{R}^{\text{cRPA}}_{\alpha\beta}(\mathbf{k};\omega)\}$ and finding implementable expressions for $\{\mathcal{I}^{\mathbf{k}}_\alpha(\mathbf{r})\}$ yields $U(\mathbf{r},\mathbf{r}';\omega)$. $\tilde{R}^{\text{cRPA}}_{\alpha\beta}(\mathbf{k},\omega)$ only depends on $\mathbf{k}\in$ IBZ and one could thus imagine using only $\mathbf{k}\in$ IBZ and rotate to BZ using known symmetries. Symmetry will however not be used in this work making some parts of the code faster, but some slower. Further, $\mathbf{r}$ and $\mathbf{r}'$ are arbitrary, but even if in the same MT (on-site), all basis states must be used contrary to when using the naïve basis expansion. Before finding implementable expressions for $\{\mathcal{I}^{\mathbf{k}}_\alpha(\mathbf{r})\}$, the possibility of making use of symmetry will be investigated.

The transformation $v(|\mathbf{r}_2-\mathbf{r}'|) \to v(|\mathbf{r}_2-\mathbf{r}'|) + v'(\mathbf{r}')$ leaves $\widetilde{\delta\rho}^{\text{cRPA}}(\mathbf{r}_1,\mathbf{r}';\omega)$ invariant since v' is constant with respect to $\mathbf{r}_2$. Charge conservation then implies that

$$U^c(\mathbf{r},\mathbf{r}';\omega) \to \int d^3r_1 \left[v(|\mathbf{r}-\mathbf{r}_1|) + v'(\mathbf{r}')\right] \widetilde{\delta\rho}^{\text{cRPA}}(\mathbf{r}_1,\mathbf{r}';\omega) = U^c(\mathbf{r},\mathbf{r}';\omega).$$

$\mathcal{I}^{\mathbf{k}}_\alpha(\mathbf{r})$ is further affected by a constant. So, ignoring constants in $\mathcal{I}^{\mathbf{k}}_\alpha(\mathbf{r})$ does not affect $U^c(\mathbf{r},\mathbf{r}';\omega)$, a conclusion that will be used in the coming derivation. The focus will now be on obtaining implementable expressions for the interactions $\{\mathcal{I}^{\mathbf{k}}_\alpha(\mathbf{r})\}$.

3.3.1 Muffin-Tin Interactions

MT and IR interactions must be treated separately, starting with the former, where α is the combined index $aLMP$ and MT(α) $\equiv$ MT(a). Bloch's theorem applied on 3.2 implies

$$\mathcal{I}^{\mathbf{k}}_\alpha(\mathbf{r}) = \int_{\text{MT}(\alpha)} d^3r_\alpha \sum_{\mathbf{T}} \frac{\mathrm{e}^{i\mathbf{k}\cdot\mathbf{T}}}{|\mathbf{r}_\alpha + \mathbf{R}_\alpha + \mathbf{T} - \mathbf{r}|} B^{\mathbf{k}}_\alpha(\mathbf{r}_\alpha + \mathbf{R}_\alpha).$$

Here, $\mathbf{r}_\alpha + \mathbf{R}_\alpha = \mathbf{r}_1$ where $\mathbf{R}_\alpha$ points to the atom of combined index α and

$$B^{\mathbf{k}}_\alpha(\mathbf{r}_\alpha + \mathbf{R}_\alpha) = \mathrm{e}^{i\mathbf{k}\cdot\mathbf{R}_\alpha} b_\alpha(r_\alpha) Y_{l_\alpha m_\alpha}(\hat{\mathbf{r}}_\alpha)$$

where b_α is available in *SPEX*. Due to the long-ranged behavior $\sim 1/|\mathbf{r}-\mathbf{T}|$, the integral is impossible to calculate directly, and Ewald summation is called for, where [19]

$$\begin{aligned} \sum_{\mathbf{T}} \frac{\mathrm{e}^{i\mathbf{k}\cdot\mathbf{T}}}{|\mathbf{r}-\mathbf{r}_1-\mathbf{T}|} = \frac{4\pi}{\Omega} \left[\sum_{\mathbf{G}\neq-\mathbf{k}} \frac{\mathrm{e}^{-|\mathbf{k}+\mathbf{G}|^2/4\alpha^2}}{|\mathbf{k}+\mathbf{G}|^2} \mathrm{e}^{i(\mathbf{k}+\mathbf{G})\cdot(\mathbf{r}-\mathbf{r}_1)} + \lim_{|\mathbf{k}+\mathbf{G}|\to 0} \frac{\mathrm{e}^{-|\mathbf{k}+\mathbf{G}|^2/4\alpha^2}}{|\mathbf{k}+\mathbf{G}|^2} \right] \\ + \alpha \sum_{\mathbf{T}} \frac{\mathrm{erfc}(\alpha|\mathbf{r}-\mathbf{r}_1-\mathbf{T}|)}{\alpha|\mathbf{r}-\mathbf{r}_1-\mathbf{T}|} \mathrm{e}^{i\mathbf{k}\cdot\mathbf{T}}. \end{aligned} \tag{3.3}$$

α is chosen to give rather short-ranged behavior in both $|\mathbf{r}-\mathbf{T}|$ and $|\mathbf{k}+\mathbf{G}|$. The second term, only present when both $\mathbf{G}=\mathbf{0}$ and $\mathbf{k}=\mathbf{0}$, is constant and can thus be ignored according to above arguments. With $\mathcal{I}_\alpha^{\mathbf{k}}(\mathbf{r})=\mathcal{I}_\alpha^{\mathbf{k}(1)}(\mathbf{r})+\mathcal{I}_\alpha^{\mathbf{k}(2)}(\mathbf{r})$ resulting from the $\mathbf{G}$- and $\mathbf{T}$-terms in 3.3 respectively, the former reads (with $A_{\mathbf{kG}\alpha}\equiv 4\pi/\Omega\times\exp(-|\mathbf{k}+\mathbf{G}|^2/4\alpha^2)/|\mathbf{k}+\mathbf{G}|^2$)

$$\mathcal{I}_\alpha^{\mathbf{k}(1)}(\mathbf{r})=\int_{\mathrm{MT}(\alpha)} dr_\alpha r_\alpha^2 d\Omega_\alpha \sum_{\mathbf{G}\neq-\mathbf{k}} A_{\mathbf{kG}\alpha}\mathrm{e}^{-i(\mathbf{k}+\mathbf{G})\cdot\mathbf{r}_\alpha}B_\alpha^{\mathbf{k}}(\mathbf{r}_\alpha+\mathbf{R}_\alpha)\mathrm{e}^{i(\mathbf{k}+\mathbf{G})\cdot(\mathbf{r}-\mathbf{R}_\alpha)}.$$

Using [20]

$$\mathrm{e}^{-i(\mathbf{k}+\mathbf{G})\cdot\mathbf{r}_\alpha}=4\pi\sum_{l=0}^{\infty}(-i)^l j_l(|\mathbf{k}+\mathbf{G}|r_\alpha)\sum_{m=-l}^{l}Y_{lm}^*(\hat{\mathbf{r}}_\alpha)Y_{lm}(\widehat{\mathbf{k}+\mathbf{G}})$$

and orthonormality $\int d\Omega_\alpha Y_{lm}^*(\hat{\mathbf{r}}_\alpha)Y_{l_\alpha m_\alpha}(\hat{\mathbf{r}}_\alpha)=\delta_{l,l_\alpha}\delta_{m,m_\alpha}$ results in

$$\mathcal{I}_\alpha^{\mathbf{k}(1)}(\mathbf{r})=4\pi(-i)^{l_\alpha}\int_{\mathrm{MT}(\alpha)} dr_\alpha r_\alpha^2 b_\alpha(r_\alpha)\sum_{\mathbf{G}\neq-\mathbf{k}} A_{\mathbf{kG}\alpha}j_{l_\alpha}(|\mathbf{k}+\mathbf{G}|r_R)Y_{l_\alpha m_\alpha}(\widehat{\mathbf{k}+\mathbf{G}})\mathrm{e}^{i(\mathbf{k}+\mathbf{G})\cdot\mathbf{r}}.$$

$\mathcal{I}_\alpha^{\mathbf{k}(2)}(\mathbf{r})$ further reads (with $\mathbf{r}_T=\mathbf{r}-\mathbf{R}_\alpha-\mathbf{T}$)

$$\mathcal{I}_\alpha^{\mathbf{k}(2)}(\mathbf{r})=\alpha\int_\alpha dr_\alpha r_\alpha^2 d\Omega_\alpha\sum_{\mathbf{T}}\frac{\mathrm{erfc}(\alpha|\mathbf{r}_\alpha-\mathbf{r}_T|)}{\alpha|\mathbf{r}_\alpha-\mathbf{r}_T|}\mathrm{e}^{i\mathbf{k}\cdot\mathbf{T}}B_\alpha^{\mathbf{k}}(\mathbf{r}_\alpha+\mathbf{R}_\alpha).$$

Restricting $\mathbf{r}$ to the first unit cell, for some lattice vectors $\mathbf{T}$ there is a point $\mathbf{r}_\alpha$ such that $|\mathbf{r}_\alpha-\mathbf{r}_T|\to 0$, which yields a divergence and requires special treatment. Trivial terms, denoted $t.t.$, with no divergence are directly integrated by Gaussian integration. Using [19]

$$\frac{\mathrm{erfc}(\alpha|\mathbf{r}_\alpha-\mathbf{r}_T|)}{\alpha|\mathbf{r}_\alpha-\mathbf{r}_T|}=\sum_{l=0}^{\infty}\frac{4\pi}{2l+1}\left[\frac{r_<^l}{\alpha r_>^{l+1}}-g_l(r_\alpha,r_T)\right]\sum_{m=-l}^{l}Y_{lm}^*(\hat{\mathbf{r}}_\alpha)Y_{lm}(\hat{\mathbf{r}}_T)$$

for the other terms ($r_<=\min(r_\alpha,r_T)$, $r_>=\max(r_\alpha,r_T)$) and orthonormality yields

$$\mathcal{I}_\alpha^{\mathbf{k}(2)}(\mathbf{r})=\frac{4\pi\alpha}{2l_\alpha+1}\int_\alpha dr_\alpha r_\alpha^2 b_\alpha(r_\alpha)\sum_{\mathbf{T}}^{\text{non-triv.}}\left[\frac{r_<^{l_\alpha}}{\alpha r_>^{l_\alpha+1}}-g_{l_\alpha}(r_\alpha,r_T)\right]Y_{l_\alpha m_\alpha}(\hat{\mathbf{r}}_T)\mathrm{e}^{i\mathbf{k}\cdot(\mathbf{R}_\alpha+\mathbf{T})}+t.t.$$

where Gaussian integration (see [19]) is applied on

$$\frac{4\pi}{2l_\alpha+1}g_{l_\alpha}(r_\alpha,r_T)Y_{l_\alpha m_\alpha}(\hat{\mathbf{r}}_T)=\int d\Omega_\alpha\frac{\mathrm{erf}(\alpha|\mathbf{r}_\alpha-\mathbf{r}_T|)}{\alpha|\mathbf{r}_\alpha-\mathbf{r}_T|}Y_{l_\alpha m_\alpha}(\hat{\mathbf{r}}_\alpha).$$

3.3.2 Interstitial Interactions

For the IR interactions the tedious geometry of the IR is circumvented by extending

$$B_{\mathbf{G}}^{\mathbf{k}}(\mathbf{r}_1)=\frac{1}{\sqrt{\Omega}}\mathrm{e}^{i(\mathbf{k}+\mathbf{G})\cdot\mathbf{r}_1}$$

to all of space, integrating, and subtracting the MT's as follows:

$$\mathcal{I}_{\mathbf{G}}^{\mathbf{k}}(\mathbf{r})=\int d^3r_1\frac{1}{|\mathbf{r}_1-\mathbf{r}|}B_{\mathbf{G}}^{\mathbf{k}}(\mathbf{r}_1)-\sum_{\mathbf{R}_\alpha}\int_{\mathrm{MT}(\alpha)}d^3r_\alpha\sum_{\mathbf{T}}\frac{\mathrm{e}^{i\mathbf{k}\cdot\mathbf{T}}}{|\mathbf{r}_\alpha+\mathbf{R}_\alpha+\mathbf{T}-\mathbf{r}|}B_{\mathbf{G}}^{\mathbf{k}}(\mathbf{r}_\alpha+\mathbf{R}_\alpha).$$

The first term is a simple Fourier transform, and reads

$$\mathcal{I}_{\mathbf{G}}^{\mathbf{k}(1)}(\mathbf{r})=\frac{4\pi}{\sqrt{\Omega}|\mathbf{k}+\mathbf{G}|^2}\mathrm{e}^{i(\mathbf{k}+\mathbf{G})\cdot\mathbf{r}}.$$

$\mathbf{k}=\mathbf{G}=\mathbf{0}$ yields a constant, and is thus removed. The rest is split into $\mathcal{I}_{\mathbf{G}}^{\mathbf{k}(2)}(\mathbf{r})+\mathcal{I}_{\mathbf{G}}^{\mathbf{k}(3)}(\mathbf{r})$ for $\mathbf{G}$- and $\mathbf{T}$-terms from the Ewald summation respectively. $\mathcal{I}_{\mathbf{G}}^{\mathbf{k}(2)}(\mathbf{r})$ takes the form

$$\mathcal{I}^{\mathbf{k}(2)}_{\mathbf{G}}(\mathbf{r}) = -\sum_{\mathbf{R}_\alpha}\int_{\text{MT}(\alpha)} dr_\alpha r_\alpha^2 d\Omega_\alpha \sum_{\mathbf{G}'\neq -\mathbf{k}} A_{\mathbf{k}\mathbf{G}'\alpha} \mathrm{e}^{i(\mathbf{G}-\mathbf{G}')\cdot\mathbf{r}_\alpha}\frac{1}{\sqrt{\Omega}}\mathrm{e}^{i(\mathbf{k}+\mathbf{G}')\cdot\mathbf{r}}\mathrm{e}^{i(\mathbf{G}-\mathbf{G}')\cdot\mathbf{R}_\alpha}.$$

Expanding $\mathrm{e}^{i(\mathbf{G}-\mathbf{G}')\cdot\mathbf{r}_R}$ as before and using $\int d\Omega_\alpha Y^*_{lm}(\hat{\mathbf{r}}_\alpha) = \sqrt{4\pi}\delta_{l0}\delta_{m0}$ implies

$$\mathcal{I}^{\mathbf{k}(2)}_{\mathbf{G}}(\mathbf{r}) = -4\pi\sum_{\mathbf{R}_\alpha}\int_{\text{MT}(\alpha)} dr_\alpha r_\alpha^2 \sum_{\mathbf{G}'\neq -\mathbf{k}} A_{\mathbf{k}\mathbf{G}'\alpha} j_0(|\mathbf{G}-\mathbf{G}'|r_\alpha)\frac{1}{\sqrt{\Omega}}\mathrm{e}^{i(\mathbf{k}+\mathbf{G}')\cdot\mathbf{r}}\mathrm{e}^{i(\mathbf{G}-\mathbf{G}')\cdot\mathbf{R}_\alpha}.$$

For $\mathcal{I}^{\mathbf{k}(3)}_{\mathbf{G}}(\mathbf{r})$, just as for $\mathcal{I}^{\mathbf{k}(2)}_{\alpha}(\mathbf{r})$, only some $\mathbf{T}$-terms require expansions. Thus,

$$\mathcal{I}^{\mathbf{k}(3)}_{\mathbf{G}}(\mathbf{r}) = -\alpha\sum_{\mathbf{R}_\alpha}\int_{\text{MT}(\alpha)} dr_\alpha r_\alpha^2 d\Omega_\alpha \sum_{\mathbf{T}}^{\text{non-triv.}} \frac{\text{erfc}(\alpha|\mathbf{r}_\alpha-\mathbf{r}_T|)}{\alpha|\mathbf{r}_\alpha-\mathbf{r}_T|}\frac{1}{\sqrt{\Omega}}\mathrm{e}^{i(\mathbf{k}+\mathbf{G})\cdot(\mathbf{r}_\alpha+\mathbf{R}_\alpha+\mathbf{T})} + t.t.$$

Expanding $\text{erfc}(\alpha|\mathbf{r}_\alpha-\mathbf{r}_T|)/(\alpha|\mathbf{r}_\alpha-\mathbf{r}_T|)$ and $\mathrm{e}^{i(\mathbf{k}+\mathbf{G})\cdot\mathbf{r}_\alpha}$ and using orhonormality implies

$$\mathcal{I}^{\mathbf{k}(3)}_{\mathbf{G}}(\mathbf{r}) = -\frac{(4\pi)^2\alpha}{\sqrt{\Omega}}\sum_{\mathbf{R}_\alpha}\int_{\text{MT}(\alpha)} dr_\alpha r_\alpha^2 \sum_{\mathbf{T}}^{\text{non-triv.}}\sum_{l=0}^{\infty}\frac{i^l}{2l+1}\left[\frac{r_<^l}{\alpha r_>^{l+1}} - g_l(r_\alpha, r_T)\right] j_l(|\mathbf{k}+\mathbf{G}|r_\alpha)$$
$$\times \sum_{m=-l}^{l} Y_{lm}(\hat{\mathbf{r}}_T) Y^*_{lm}(\widehat{\mathbf{k}+\mathbf{G}})\mathrm{e}^{i(\mathbf{k}+\mathbf{G})\cdot(\mathbf{R}_\alpha+\mathbf{T})} + t.t.$$

where only terms with $l \leq 4$ are kept since quickly decaying in r_α for large l. Let once again α label both MT- and IR-states. Once $\mathcal{I}^{\mathbf{k}}_{\alpha}(\mathbf{r})$ is properly implemented, $\tilde{R}^{\text{cRPA}}(\mathbf{r},\mathbf{r}';\omega)$ and $\widetilde{\delta\rho}^{\text{cRPA}}(\mathbf{r},\mathbf{r}';\omega)$ are given by ($U^c(\mathbf{r},\mathbf{r}';\omega)$ is included for completeness)

$$\tilde{R}^{\text{cRPA}}(\mathbf{r},\mathbf{r}';\omega) = \sum_{\mathbf{k}\in\text{BZ}} w_{\mathbf{k}} \sum_{\alpha\beta} B^{\mathbf{k}}_{\alpha}(\mathbf{r})\tilde{R}^{\text{cRPA}}_{\alpha\beta}(\mathbf{k};\omega)B^{\mathbf{k}*}_{\beta}(\mathbf{r}')$$
$$\widetilde{\delta\rho}^{\text{cRPA}}(\mathbf{r},\mathbf{r}';\omega) = \sum_{\mathbf{k}\in\text{BZ}} w_{\mathbf{k}} \sum_{\alpha\beta} B^{\mathbf{k}}_{\alpha}(\mathbf{r})\tilde{R}^{\text{cRPA}}_{\alpha\beta}(\mathbf{k};\omega)\mathcal{I}^{\mathbf{k}*}_{\beta}(\mathbf{r}')$$
$$U^c(\mathbf{r},\mathbf{r}';\omega) = \sum_{\mathbf{k}\in\text{BZ}} w_{\mathbf{k}} \sum_{\alpha\beta} \mathcal{I}^{\mathbf{k}}_{\alpha}(\mathbf{r})\tilde{R}^{\text{cRPA}}_{\alpha\beta}(\mathbf{k};\omega)\mathcal{I}^{\mathbf{k}*}_{\beta}(\mathbf{r}').$$

As pointed out earlier, the contribution from the Γ-point, $\Gamma = (0,0,0)$, requires a different treatment than other $\mathbf{k}$-points, with $w_{\mathbf{k}\neq\Gamma} = 1/N_{\mathbf{k}}$. Since this is the last step needed to obtain $U(\mathbf{r},\mathbf{r}';\omega)$, the next section deals with this issue.

3.4 Γ-Point Treatment

In the limit $k \to 0$ v goes as $1/k^2$ and $\tilde{R}^{\text{cRPA}} = \tilde{P}^{\text{r0}} + \tilde{P}^{\text{r0}}v\tilde{P}^{\text{r0}} + \ldots$ goes (like $\tilde{P}^{\text{r0}}$) as k^2. On matrix form $U^c = v\tilde{R}^{\text{cRPA}}v$, which means that also U^c goes like $1/k^2$ in the limit $k \to 0$. Due to the anisotropic crystal structure the limit is also influenced by the direction of $\mathbf{k}$. Let $U^c(\omega)$ denote $U^c(\mathbf{r},\mathbf{r}';\omega)$ and $U^c(\mathbf{k};\omega)$ denote $\sum_{\alpha\beta}\mathcal{I}^{\mathbf{k}}_{\alpha}(\mathbf{r})\tilde{R}^{\text{cRPA}}_{\alpha\beta}(\mathbf{k};\omega)\mathcal{I}^{\mathbf{k}*}_{\beta}(\mathbf{r}')$ for any given $\mathbf{r}$ and $\mathbf{r}'$, so that $U^c(\omega) = \sum_{\mathbf{k}\in\text{BZ}} w_{\mathbf{k}}U^c(\mathbf{k};\omega)$. In spherical coordinates, $\mathbf{k} = (k,\theta_k,\varphi_k)$, according to the above, $U^c(\mathbf{k};\omega)$ goes like $f(\theta_k,\varphi_k)/k^2$ in the limit $k \to 0$. It thus diverges at the Γ-point, but yields a finite value using integration instead of summation over $\mathbf{k}$. This short section will present two different schemes to treat the Γ-point using integrals.

In the first (less exact) scheme, define $\bar{f} = \frac{1}{26}\sum_{n=1}^{26} k_n^2 U^c(\mathbf{k}_n;\omega)$ where $\{\mathbf{k}_n\}$ are the 26 Γ-point neighbours on a parallelepiped. Let $\mathbf{k}_1$, $\mathbf{k}_2$ and $\mathbf{k}_3$ be three unit-direction neighbours and define a sphere around Γ with volume $\Delta V = |(\mathbf{k}_1\times\mathbf{k}_2)\cdot\mathbf{k}_3| = 4\pi\bar{k}_{nn}^3/3 = \Omega_{\text{BZ}}/N_{\mathbf{k}} = \Omega_{\text{BZ}}w_{\mathbf{k}\neq\Gamma}$. Then the Γ-point contribution is approximated as

$$w_\Gamma U^c(\Gamma;\omega) \approx \frac{1}{\Omega_{\rm BZ}}\int_{\Delta V} d^3k \frac{\bar{f}}{k^2} = \frac{4\pi \bar{k}_{nn}\bar{f}}{\Omega_{\rm BZ}} = \frac{3}{26}\left(\frac{4\pi\bar{k}_{nn}^3}{3\Omega_{\rm BZ}}\right)\sum_{n=1}^{26}\left(\frac{k_n}{\bar{k}_{nn}}\right)^2 U^c(\mathbf{k}_n;\omega)$$
$$= \frac{3}{26}\sum_{n=1}^{26}\left(\frac{k_n}{\bar{k}_{nn}}\right)^2 w_{\mathbf{k}_n} U^c(\mathbf{k}_n;\omega).$$

A second, more exact scheme (see [18]) is used in this work, replacing the integral as follows

$$\frac{1}{\Omega_{\rm BZ}}\int_{\Delta V} d^3k \frac{\bar{f}}{k^2} \rightsquigarrow \frac{1}{\Omega_{\rm BZ}}\int_{\rm BZ} d^3k \frac{\bar{f}}{k^2} - \frac{1}{N_{\mathbf{k}}}\sum_{\mathbf{k}\neq\Gamma}\frac{\bar{f}}{k^2}$$

which by construction obeys

$$\sum_{\mathbf{k}\in{\rm BZ}} w_{\mathbf{k}}\frac{\bar{f}}{k^2} = \frac{1}{\Omega_{\rm BZ}}\int_{\rm BZ} d^3k \frac{\bar{f}}{k^2}.$$

3.5 From $U(\mathbf{r},\mathbf{r}';\omega)$ to $U(\mathbf{r},\mathbf{r}';\tau)$

Since the spatial grid (in-plane $\mathbf{r}$ for fix $\mathbf{r}'$) used is only 25×25 it is cheaper to transform $U(\mathbf{r},\mathbf{r}';\omega)$ to time than $\tilde{R}^{\rm cRPA}_{\alpha\beta}(\mathbf{k};\omega)$. U is the time-ordered interaction and obeys the Kramers-Kronig relation in the frequency domain but not in time-domain, where it is easy to show that it is the retarded interaction U^r that obeys this relation. $U^r(\mathbf{r},\mathbf{r}';\omega)$ fulfils (given in [21] for R^r but is valid also for U^r)

$$\text{Re } U^r(\mathbf{r},\mathbf{r}';\omega) = \text{Re } U(\mathbf{r},\mathbf{r}';\omega)$$
$$\text{Im } U^r(\mathbf{r},\mathbf{r}';\omega) = \text{Im } U(\mathbf{r},\mathbf{r}';\omega)\times \text{sgn}(\omega).$$

Inverse Fourier transformation of U^r from frequency to time-delay (retardation) $\tau = t - t'$ yields (dropping the supscript r in the time-domain)

$$U(\mathbf{r},\mathbf{r}';\tau) = v(|\mathbf{r}-\mathbf{r}'|)\delta(\tau) + \int\frac{d\omega}{2\pi}U^{cr}(\mathbf{r},\mathbf{r}';\omega)\mathrm{e}^{-i\omega\tau}.$$

$U(\mathbf{r},\mathbf{r}';\tau)$ is the response to an impulse at $\tau = 0$, in the non-relativistic limit with instantaneous bare interaction. The instantaneous perturbation probes the system - you cannot hold down a guitar string and expect music. The first instantaneous term is like hitting a guitar string, and the second retarded term like the following oscillations of the string (the music). Note that U in the time-domain has dimension [energy/time] rather than [energy]. A useful relation for this conversion (where H denotes the energy-unit Hartree) is $\mathrm{H}^{-1} \approx 152.26\,\mathrm{as}$ (based on [22]). Since the real- and imaginary-part of U^{cr} are even in ω it follows that Re $U^{cr}(\mathbf{r},\mathbf{r}';\omega)$ transforms to Re $U^c(\mathbf{r},\mathbf{r}';\tau)$. In the result section U^c denotes the real-part. In *SPEX*, U^{cr} is obtained for discrete ω_i, $i = 1,\ldots,N$ where $\omega_1 = 0$ and ω_N is big enough to yield imaginary parts of U^c close to 0 ($\omega_N = 10\,\mathrm{H}$ is used). The integral is then split (using the even symmetry)

$$\text{Re}\,U^c(\mathbf{r},\mathbf{r}';\tau) = \sum_{i=1}^{N-1}\int_{\omega_i}^{\omega_{i+1}}\frac{d\omega}{\pi}\text{Re}\,U_i^{cr}(\mathbf{r},\mathbf{r}';\omega)\cos\omega\tau + \int_{\omega_N}^{\infty}\frac{d\omega}{\pi}\text{Re}\,U_e^{cr}(\mathbf{r},\mathbf{r}';\omega)\cos\omega\tau.$$

Re $U_i^{cr}(\mathbf{r},\mathbf{r}';\omega)$ is a linear interpolation using Re $U^{cr}(\mathbf{r},\mathbf{r}';\omega_i)$ and Re $U^{cr}(\mathbf{r},\mathbf{r}';\omega_{i+1})$, allowing for partial integration (Filon's method). Re $U_e^{cr}(\mathbf{r},\mathbf{r}';\omega > \omega_N)$ is an extrapolation using Re $U^{cr}(\mathbf{r},\mathbf{r}';\omega_N)$ and that Re $U^{cr}(\mathbf{r},\mathbf{r}';\omega)$ goes like $1/\omega$ for large ω.

3.6 Execution Times

The symmetries associated with the rotation of $\mathbf{k}$ from the irreducible to the full BZ is not utilized, meaning that $N_\alpha \times N_\mathbf{k}$ different $\mathcal{I}^\mathbf{k}_\alpha(\mathbf{r})$ are calculated, where N_α and $N_\mathbf{k}$ are the number of MPB functions and number of $\mathbf{k}$-mesh points in the full BZ respectively. Since a 4×4×4-mesh is used, $N_\mathbf{k} = 64$. The number of MPB functions (for La_2CuO_4) is about 600 in the MTs and 400 in the IR for a typical $\mathbf{k}$, so that $N_\alpha \approx 1000$, meaning that about 64000 Ewald summations need to be performed.

Still, in this work, this has not been a big obstacle due to the access to a cluster with a large amount of nodes, out of which 7 was used, each with 6 cores with 2 threads each, with a CPU speed of 3.7 GHz. The computational time for one $\mathbf{k}$ contribution (for La_2CuO_4) was spent roughly as follows:

- (∼30 % ↔ 1.8 hours) Obtaining the matrix elements $\tilde{R}^{\text{cRPA}}_{\alpha\beta}(\mathbf{k},\omega)$ for all α, β and ω.

- (∼65 % ↔ 3.9 hours) Calculating $\mathcal{I}^\mathbf{k}_\alpha(\mathbf{r})$ for all α.

- (∼ 5 % ↔ 0.3 hours) Performing $\sum_{\alpha\beta} \mathcal{I}^\mathbf{k}_\alpha(\mathbf{r})\tilde{R}^{\text{cRPA}}_{\alpha\beta}(\mathbf{k};\omega)\mathcal{I}^{\mathbf{k}*}_\beta(\mathbf{r}')$ for all ω.

Once all $\mathbf{k}$-contributions (except the Γ-point) were calculated the Gamma-point treatment and Fourier transformation to $U(\mathbf{r},\mathbf{r}';\tau)$ just took a few seconds each.

Chapter 4

Results and Discussion

To test the implementation W will first be presented for Ni, and comparisons will be made with earlier results from [8], based on the linear muffin-tin orbital (LMTO) method. Then, the fully screened interaction W (within RPA) will be compared for La_2CuO_4 and $SrVO_3$. Within LDA La_2CuO_4 becomes a metal just like $SrVO_3$. This, and that the $\mathbf{k}$-dependence of the band structure is constrained by the crystal symmetry motivates that the LDA based calculations mimic the doped system, with a metallic normal state. This will be followed by a more detailed study of the partially screened interactions (U_1 and U_3) of La_2CuO_4 within the one- and three-band models defined in section 2.3.

4.1 Ni

The Ni unit cell contains a single Ni atom at $(0,0,0)$. The fcc lattice vectors are $\mathbf{T}_1 = 3.325(0,1,1)\,\mathrm{au}$, $\mathbf{T}_2 = 3.325(1,0,1)\,\mathrm{au}$ and $\mathbf{T}_3 = 3.325(1,1,0)\,\mathrm{au}$. [23] Since Ni is only a test material the LDA band structure will not be presented, but in figure 4.1 the static values of R, $\delta\rho$, W^c and W are shown along the $(1,0,0)$-direction for a test charge at $(0,0,0)$.

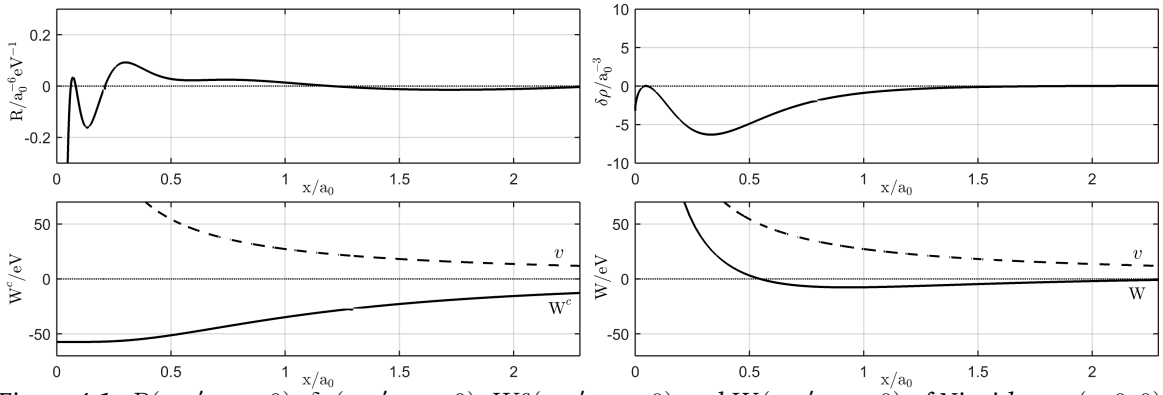

Figure 4.1: $R(\mathbf{r},\mathbf{r}',\omega=0)$, $\delta\rho(\mathbf{r},\mathbf{r}',\omega=0)$, $W^c(\mathbf{r},\mathbf{r}',\omega=0)$ and $W(\mathbf{r},\mathbf{r}',\omega=0)$ of Ni with $\mathbf{r}=(x,0,0)$ and $\mathbf{r}'=(0,0,0)\,\mathrm{au}$.

The LMTO results in [8] for W are reproduced to a degree that it appears the same. This does not only mean that the implementation in this work seems to be correct, it also means that LMTO may be a good approximation for these kind of calculations. The results illustrate that $\delta\rho$ is a smearing of R (spatial convolution between v and R) and that W^c further is a smearing of $\delta\rho$. Note the attractive region (where W is negative). Keep in mind that RPA is used. Due to the weak correlations in Ni, this may be fine for W, but for the La_2CuO_4 this is only well-motivated for U_1 and U_3 when removing the d-d screening channel.

4.2 $SrVO_3$ vs La_2CuO_4

The reader is encouraged to revisit the crystal structures and LDA band structures of La_2CuO_4 and $SrVO_3$ (Fig. 2.2) before continuing. With $T_S = 7.26\,\text{au}$ (S for $SrVO_3$), the cubic lattice vectors of $SrVO_3$ are $\mathbf{T}_1 = T_S(1,0,0)$, $\mathbf{T}_2 = T_S(0,1,0)$ and $\mathbf{T}_3 = T_S(0,0,1)$. The unit cell contains V at $(0,0,0)$, Sr at $T_S(0.5,0.5,0.5)$ and O at $T_S(0.5,0,0)$, $T_S(0,0.5,0)$ and $T_S(0,0,0.5)$. [24] With $T_L = 7.212\,\text{au}$ (L for La_2CuO_4), the lattice vectors of La_2CuO_4 are $\mathbf{T}_1 = T_L(1,0,0)$, $\mathbf{T}_2 = T_L(0,1,0)$ and $\mathbf{T}_3 = T_L(0.5,0.5,1.72835)$. The unit cell contains Cu at $(0,0,0)$, La at $\pm T_L(0.5,0.5,0.477)$ and O at $T_L(0.5,0,0)$, $T_L(0,0.5,0)$ and $T_L(0,0,\pm 0.5)$. [25] All plots for $SrVO_3$ and La_2CuO_4 will be in the xy$(0,0,0)$ plane in the first unit cell. So, $(x,y) \in ([0,T_S],[0,T_S])$ in the VO_2 plane of $SrVO_3$ and $(x,y) \in ([0,T_L],[0,T_L])$ in the CuO_2 plane of La_2CuO_4. The in-plane valence density $\rho(\mathbf{r})$ is plotted for $SrVO_3$ and La_2CuO_4 together with the in-plane crystal structure (Fig. 4.2). Since Cu has the configuration $[Ar]4s^1 3d^{10}$ and V has $[Ar]3d^3 4s^2$ the density is higher at Cu in La_2CuO_4 than at V in $SrVO_3$.

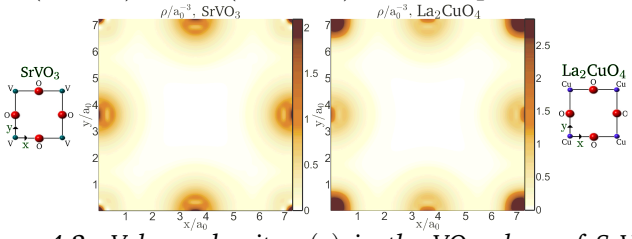

Figure 4.2: Valence density $\rho(\mathbf{r})$ in the VO_2 plane of $SrVO_3$ (left) and CuO_2 plane of La_2CuO_4 (right). The in-plane crystal structure is included next to each figure.

The static induced density $\delta\rho(\mathbf{r},\mathbf{r}',\omega=0)$ due to a test charge (electron) at $\mathbf{r}'$, which depends on this in-plane valence density (Fig. 4.2) but also on the out-of-plane electronic structure, is presented for $SrVO_3$ (Fig. 4.3) and La_2CuO_4 (Fig. 4.4). $\mathbf{r}'$ is put along a triangular path: $(0,0,0)$, $(\frac{T}{4},0,0)$, $(\frac{T}{2},0,0)$, $(\frac{T}{2},\frac{T}{4},0)$, $(\frac{T}{2},\frac{T}{2},0)$, $(\frac{T}{4},\frac{T}{4},0)$, where $T = T_S$ and T_L for $SrVO_3$ and La_2CuO_4 respectively. The point $(\frac{T}{2},\frac{T}{2},0)$ is called M (for "middle") in the following. The labels on the axes have been removed, but are the same as in Fig. 4.2. The screening at $\mathbf{r} = \mathbf{r}'$ is stronger in La_2CuO_4 than in $SrVO_3$ for all $\mathbf{r}'$. For $SrVO_3$, the on-site ($\mathbf{r} = \mathbf{r}'$) induced density at O is more negative than at V. For the latter, the electrons escape from the V d_{xy} ($\delta\rho < 0$) to the O p orbitals ($\delta\rho > 0$). With $\mathbf{r}'$ at M the electrons mainly accumulate close to O, but also on V. Also for La_2CuO_4, the on-site induced density is most negative at O, which is more polarizable than Cu. The value at Cu, however, is greater than at V in $SrVO_3$, and, due to different band symmetries, with a $d_{x^2-y^2}$-character instead of d_{xy}. The major difference from $SrVO_3$ is that the electrons accumulate effectively at both Cu and O for all $\mathbf{r}'$.

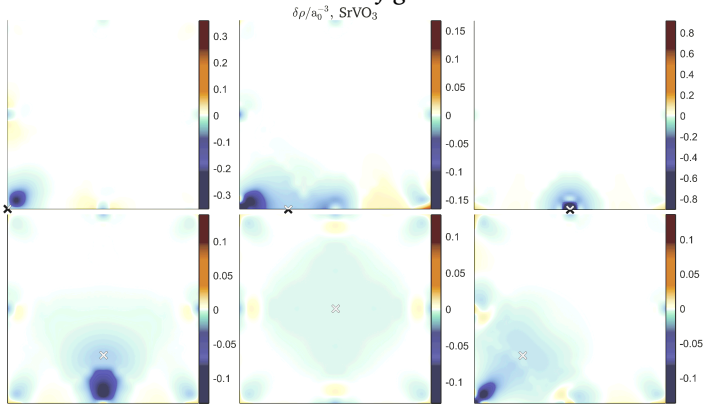

Figure 4.3: $\delta\rho(\mathbf{r},\mathbf{r}',\omega=0)$ with $\mathbf{r}$ in the VO_2 plane of $SrVO_3$. $\mathbf{r}'$ is marked by a cross.

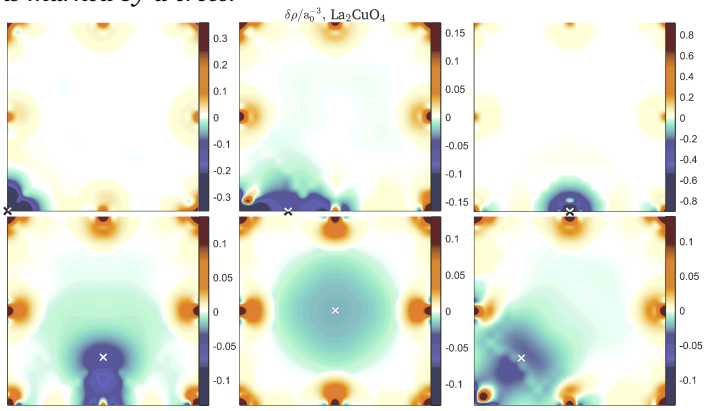

Figure 4.4: $\delta\rho(\mathbf{r},\mathbf{r}',\omega=0)$ with $\mathbf{r}$ in the CuO_2 plane of La_2CuO_4. $\mathbf{r}'$ is marked by a cross.

Before studying $W = v + W^c$ it is instructive to compare the static R, $\delta\rho$ and W^c in both materials. This is done for $\mathbf{r}'$ at M (Fig. 4.5). The difference in $\delta\rho$ between the two materials can be explained in terms of the difference in R. For the considered test charge at M the response R is negative at V in $SrVO_3$ but positive at Cu in La_2CuO_4. There also is a more pronounced region of positive R around M in La_2CuO_4. Since $\delta\rho$ is a smearing of R (convolution between v and R) the behavior of R is mimicked in $\delta\rho$. The large positive $\delta\rho$ at both Cu and O in La_2CuO_4 comes from the more negative $\delta\rho$ close to M, which further can be explained by the more negative R in the same region. W^c, which is a further smearing of $\delta\rho$ thus naturally gets more negative (by about a factor of two) close to M in La_2CuO_4 than in $SrVO_3$, meaning that the screening is more effective. In terms of the higher valence density in La_2CuO_4 this makes perfect sense, since more electrons participate in the screening.

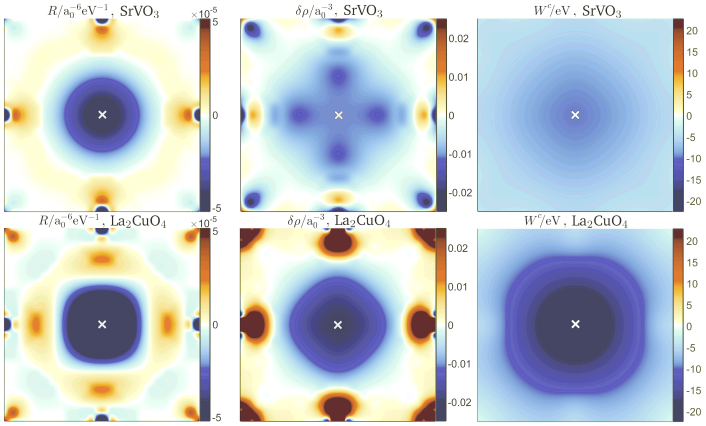

Figure 4.5: $R(\mathbf{r}, \mathbf{r}', \omega = 0)$, $\delta\rho(\mathbf{r}, \mathbf{r}', \omega = 0)$ and $W^c(\mathbf{r}, \mathbf{r}', \omega = 0)$ with $\mathbf{r}$ in the VO_2 plane of $SrVO_3$ (top) and in the CuO_2 plane of La_2CuO_4 (bottom). $\mathbf{r}'$ is marked by a cross.

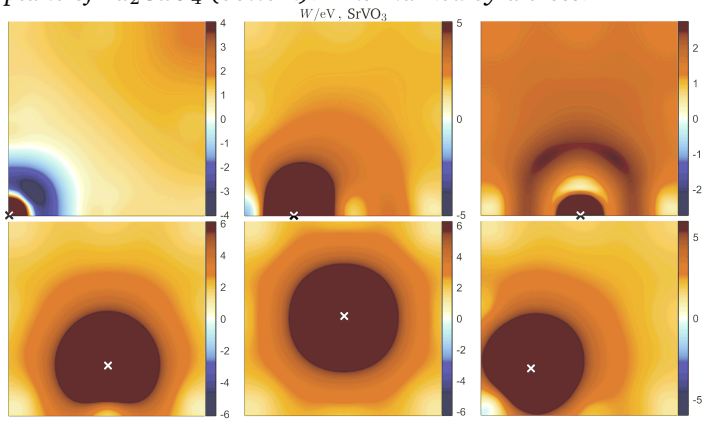

Figure 4.6: $W(\mathbf{r}, \mathbf{r}', \omega = 0)$ with $\mathbf{r}$ in the VO_2 plane of $SrVO_3$. $\mathbf{r}'$ is marked by a cross.

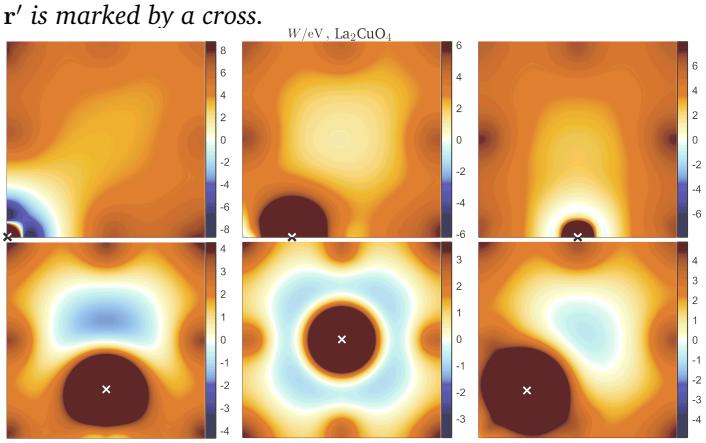

Figure 4.7: $W(\mathbf{r}, \mathbf{r}', \omega = 0)$ with $\mathbf{r}$ in the CuO_2 plane of La_2CuO_4. $\mathbf{r}'$ is marked by a cross.

Having obtained an understanding of the static W^c, the static $W = v + W^c$ will now be compared for $SrVO_3$ (Fig. 4.6) and La_2CuO_4 (Fig. 4.7), but for all $\mathbf{r}'$ along the triangular path. For La_2CuO_4 there is an attractive static interaction ($W < 0$) for several $\mathbf{r}'$, also far from Cu, but in $SrVO_3$ $\mathbf{r}'$ needs to be put close to V to give rise to attractive regions. Taking the case of $\mathbf{r}'$ at M as an example, the different magnitudes of W^c (Fig. 4.5) between the materials can explain this significant difference in the signs of W, since the same $v = 1/|\mathbf{r} - \mathbf{r}'|$ is added to both. As stated earlier, the LDA based calculations mimic the doping in La_2CuO_4, and since the doped system is known to be unstable against Cooper pairing at relatively high temperature, it is interesting that attractive regions were found to a greater extent in La_2CuO_4 than in $SrVO_3$. Still, that the calculations are based on RPA is not necessarily sufficient for W. Since this is no limitation for the partially screened interactions within a one- and three-band model, U_1

and U_3, and since these directly give the effective interaction of the electrons participating in the Cooper pairing, the next section will focus on comparing W, U_1 and U_3 in La_2CuO_4. This comparison will first be done in the static regime, and then by taking into account the dynamics ($\omega \neq 0$) and studying these quantities as a function of time.

4.3 La_2CuO_4

4.3.1 Static Interaction

Similar to W (Fig. 4.7) the effective static interactions are here presented for the one- and three-band models, U_1 (Fig. 4.8) and U_3 (Fig. 4.9), based on the earlier Wannier interpolations (Fig. 2.5). For U_1, the on-site attraction at Cu is reduced compared to that of W, and it appears that the difference between the two has mainly $d_{x^2-y^2}$ component, consistent with the character of the low-energy screening channels that have been removed in U_1. With $\mathbf{r}'$ far from Cu the difference between W and U_1 is much smaller, which indicates that the one-band subspace is made up of states mainly localized at Cu, as it should. U_3 (Fig. 4.9), contrary to U_1, displays no on-site attraction at Cu. Since the main difference between U_3 and U_1 is that the Cu d-O p screening channels have been removed in U_3 to a large extent but not in U_1 these must be responsible for the negative on-site U_1 at Cu. Just as the states in the one-band subspace were found to be localized at Cu, the same applies to the screening channel Cu d-O p, as seen by the small difference between U_1 (Fig. 4.8) and U_3 (Fig. 4.9) when $\mathbf{r}'$ is far from Cu. That this screening channel is mainly localized at Cu has already been discussed in [11]. Still, there seems to be a weak however noticable difference between U_1 and U_3 even with $\mathbf{r}'$ far from Cu.

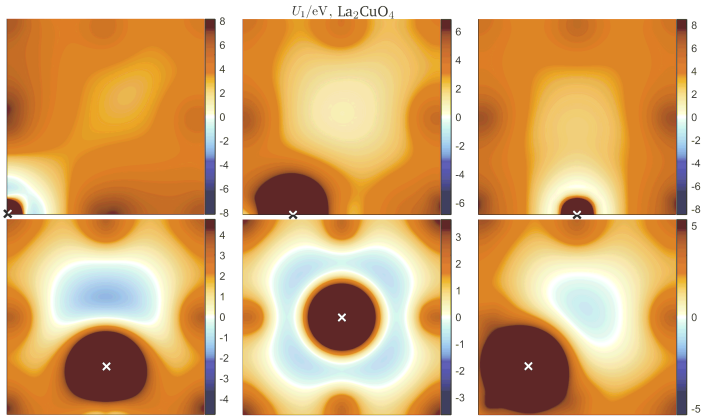

Figure 4.8: $U_1(\mathbf{r}, \mathbf{r}', \omega = 0)$ with $\mathbf{r}$ in the CuO_2 plane of La_2CuO_4. $\mathbf{r}'$ is marked by a cross.

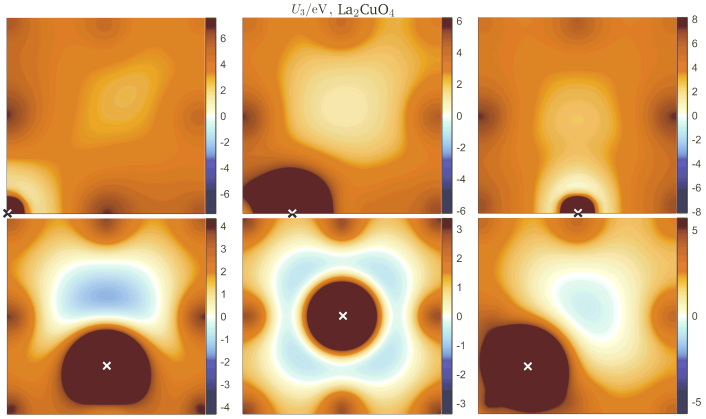

Figure 4.9: $U_3(\mathbf{r}, \mathbf{r}', \omega = 0)$ with $\mathbf{r}$ in the CuO_2 plane of La_2CuO_4. $\mathbf{r}'$ is marked by a cross.

To better account for the spatial behavior of the different screening channels the differences $W - U_1$ (Fig. 4.10), $U_1 - U_3$ (Fig. 4.11) and $W - U_3$ (Fig. 4.12) are presented in the following. $W - U_1$ is a measure of the metallic Cu d-d screening within the LDA band at the Fermi energy (within RPA), $U_1 - U_3$ of the Cu d-O p screening and $W - U_3$ is simply the sum of the two contributions.

The metallic low-energy screening $W - U_1$ (Fig. 4.10) displays visible $d_{x^2-y^2}$ orbitals at Cu, just as expected. Even when $\mathbf{r}'$ is put at O, the metallic screening is most effective at Cu. For all $\mathbf{r}'$ except at M the difference $W - U_1$ is in the order of magnitude of one or a few eV at Cu. With $\mathbf{r}'$ at M however, the $d_{x^2-y^2}$ orbital does not show up. $W - U_1$ is negative close to $\mathbf{r}'$ for all $\mathbf{r}'$, since W takes into account more screening channels. Additional screening channels do not mean that $W - U_1$ must be negative far from $\mathbf{r}'$, due to the transfer of electron density away from $\mathbf{r}'$. This explains the change of sign of $W - U_1$ a couple of atomic units away from $\mathbf{r}'$, and thus why the $d_{x^2-y^2}$ orbital at Cu is not visible with $\mathbf{r}'$ at M.

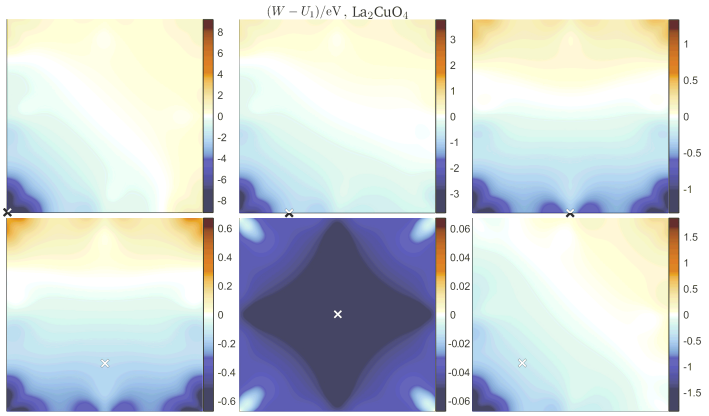

Figure 4.10: $(W - U_1)(\mathbf{r}, \mathbf{r}', \omega = 0)$ *with* $\mathbf{r}$ *in the* CuO_2 *plane of* La_2CuO_4. $\mathbf{r}'$ *is marked by a cross.*

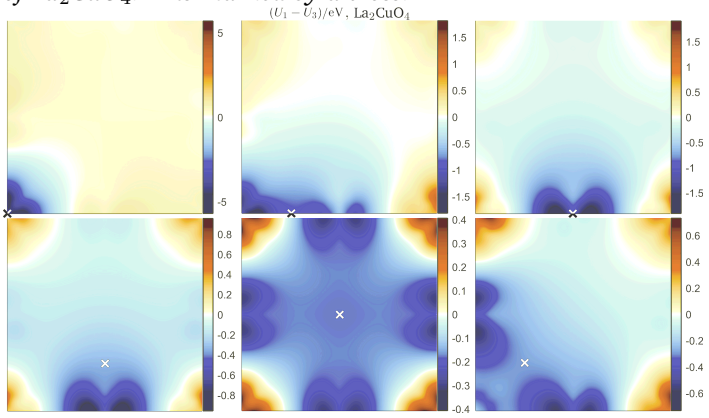

Figure 4.11: $(U_1 - U_3)(\mathbf{r}, \mathbf{r}', \omega = 0)$ *with* $\mathbf{r}$ *in the* CuO_2 *plane of* La_2CuO_4. $\mathbf{r}'$ *is marked by a cross.*

The p orbitals at O, which only appear subtly in $W - U_1$, are more involved in the Cu d-O p screening $U_1 - U_3$ (Fig. 4.11). Still, the $d_{x^2-y^2}$ orbital at Cu dominates, just as emphasized earlier and seen by doing the following comparison: With $\mathbf{r}'$ at Cu the p orbitals at O are barely visible, but with $\mathbf{r}'$ at O the $d_{x^2-y^2}$ orbitals at Cu are almost as visible as the p orbitals at O. Interestingly, the Cu d-O p screening (Fig. 4.11) is more localized at Cu than the metallic screening (Fig. 4.10). This makes sense since $W - U_1$ mainly couples electrons between Cu sites (large distance) whereas $U_1 - U_3$ between Cu and O sites (shorter distance).

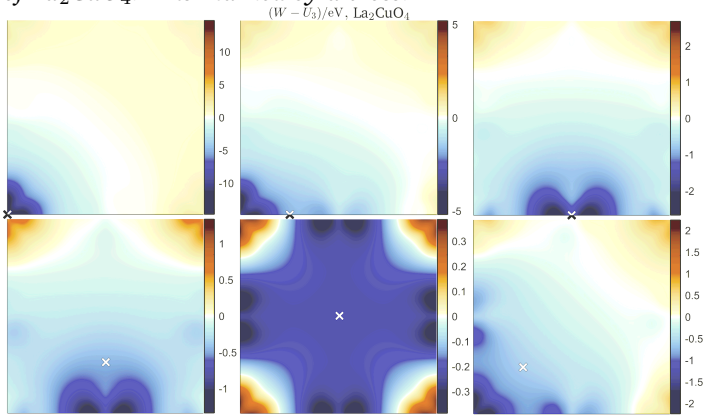

Figure 4.12: $(W - U_3)(\mathbf{r}, \mathbf{r}', \omega = 0)$ *with* $\mathbf{r}$ *in the* CuO_2 *plane of* La_2CuO_4. $\mathbf{r}'$ *is marked by a cross.*

Regarding the sum of the two channels, $W - U_3$ (Fig. 4.12) a few observations can be made. For all $\mathbf{r}'$ except when put close to Cu, $W - U_1$ and $U_1 - U_3$ display opposite signs at Cu, but the same sign at O. This results in a suppression of Cu d character and increase of O p character in $W - U_3$. Still however, the Cu d character dominates. Since short distance Cu-O transfer as well as long distance Cu-Cu transfer is included in $W - U_3$, the change of sign occurs at a distance from $\mathbf{r}'$ that is somewhere in between that of $W - U_1$ and $U_1 - U_3$.

4.3.2 Dynamical Interaction

Fig. 4.13 presents W as a function of delay τ ($= t$ with $t' = 0$) at the Cu site (row 1), the O site (row 2) and at M (row 3) for $\mathbf{r}'$ at the same positions (column 1, 2 and 3). As expected with time-reversal symmetry, interchanging $\mathbf{r}$ and $\mathbf{r}'$ does not affect W. W starts off significantly negative at $\mathbf{r} = \mathbf{r}'$, with a magnitude and behavior that is very similar at Cu and O but only about half as negative at M where also the oscillations are slower. When putting the test charge either at the Cu or O site the opposite site begins with a positive interaction, corresponding to the charge transfer between the atoms after applying the perturbation at $t = 0$. Due to the weak charge transfer to and from M, when applying the perturbation at M the interaction start off negative also at the atomic sites.

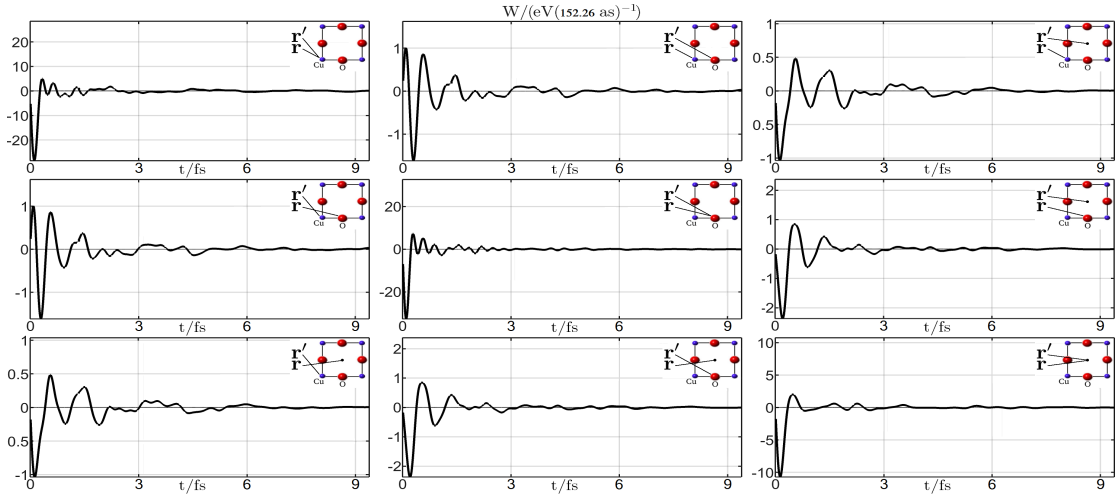

Figure 4.13: $W(\mathbf{r}, \mathbf{r}', t)$ in La_2CuO_4 with $\mathbf{r}$ and $\mathbf{r}'$ specified in each subplot. $t' = 0$.

Since the dynamics will be studied both in space and time in the following, similar plots for U_1 and U_3 are left out. However, $U_1 - U_3$ with both $\mathbf{r}$ and $\mathbf{r}'$ at Cu (Fig. 4.14) shows a decaying oscillation with $\omega \approx 9\,\mathrm{eV}$, consistent with [11].

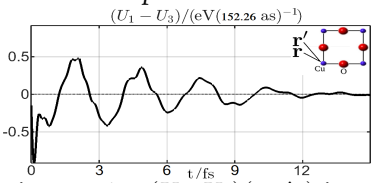

Figure 4.14: $(U_1 – U_3)(\mathbf{r},\mathbf{r}',t)$ in La_2CuO_4 with $\mathbf{r} = \mathbf{r}' = \mathbf{0}$ (at Cu). $t' = 0$.

Perturbation at Cu

To better understand W, U_1 and U_3 in space and time it is natural to first study $\delta\rho$ in space and time (Fig. 4.15). With $\mathbf{r}' = (0, 0, 0)$ (at Cu) and $t' = 0$ the electrons very quickly (attoseconds) escape this atom and accumulate at the surrounding atoms (both Cu and O). This "overpopulation" of electrons then results in further escape of electrons from these sites due to the large electron repulsion. While some electrons escape the first unit cell, some return and some enter it for the first time, which explains why $\delta\rho$ changes sign from negative to positive at the Cu site at the origin. The claim that some electrons

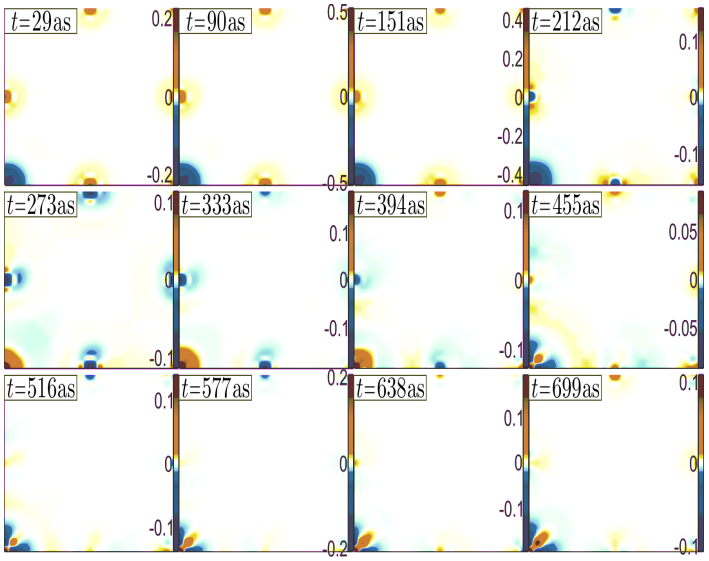

Figure 4.15: $\delta\rho(\mathbf{r}, \mathbf{r}'; t)$ (in $a_0^{-3}(152.26\,\mathrm{as})^{-1}$) with $\mathbf{r}$ in the CuO_2 plane of La_2CuO_4. $\mathbf{r}' = (0, 0, 0)$ (at Cu). $t' = 0$.

enter the first unit cell from the outside may sound counter-intuitive since $\mathbf{r}'$ was put at $(0,0,0)$, however, the perturbation at $t = 0$ goes like $1/|\mathbf{r} - \mathbf{r}'|$ and thus also affects electrons far away. In a simple picture, some electrons are reflected in each atomic layer, forcing these plasma oscillations to continue. The geometry of the electron density becomes more and more complex since each reflected electron carries information about the crystal structure (also out-of-plane). With a simple understanding of $\delta\rho$ a discussion of W (Fig. 4.16) can proceed. The main features of $\delta\rho$ are carried over to W, which starts off negative at Cu and then changes sign. After 455 attoseconds the $d_{x^2-y^2}$ orbital at Cu becomes visible, which can be traced back to $\delta\rho$ at the same time (Fig. 4.15). Just as for $\delta\rho$ the magnitude decays quite rapidly. This means that the static interaction, which is the time-integrated interaction, is mainly affected by the short-time behavior. This is quite opposite to what is usually meant by "static", where the long-time behavior is refered to. Comparisons between the short-time and static interactions will be done later.

Continuing with U_1 (Fig. 4.17), this looks very similar to W, and just as anticipated the $d_{x^2-y^2}$ orbital is still visible. Small differences can be noticed after 394 attoseconds, but it is difficult to tell whether this is due to the different scalings or not. Also U_3 (Fig. 4.18) is very similar. The main difference from W and U_1 is the absence of the $d_{x^2-y^2}$ orbital at Cu. The behavior at the neighbouring Cu sites is also quite different from that of W and U_1 after about 455 attosec-

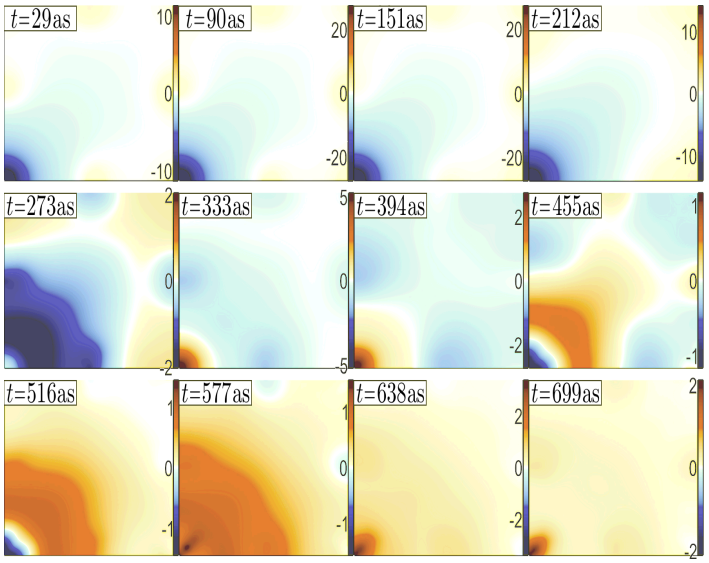

Figure 4.16: $W(\mathbf{r},\mathbf{r}';t)$ *(in* $\mathrm{eV}(152.26\,\mathrm{as})^{-1}$*) with* $\mathbf{r}$ *in the* CuO_2 *plane of* La_2CuO_4*.* $\mathbf{r}' = (0,0,0)$ *(at Cu).* $t' = 0$*.*

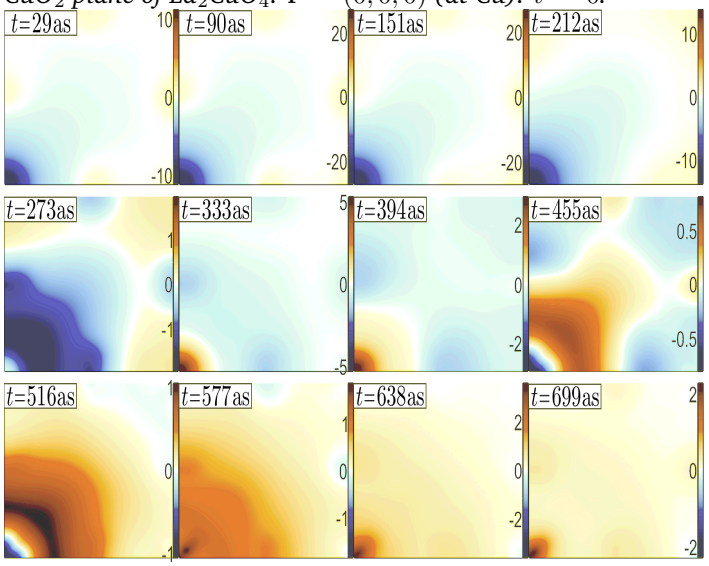

Figure 4.17: $U_1(\mathbf{r},\mathbf{r}';t)$ *(in* $\mathrm{eV}(152.26\,\mathrm{as})^{-1}$*) with* $\mathbf{r}$ *in the* CuO_2 *plane of* La_2CuO_4*.* $\mathbf{r}' = (0,0,0)$ *(at Cu).* $t' = 0$*.*

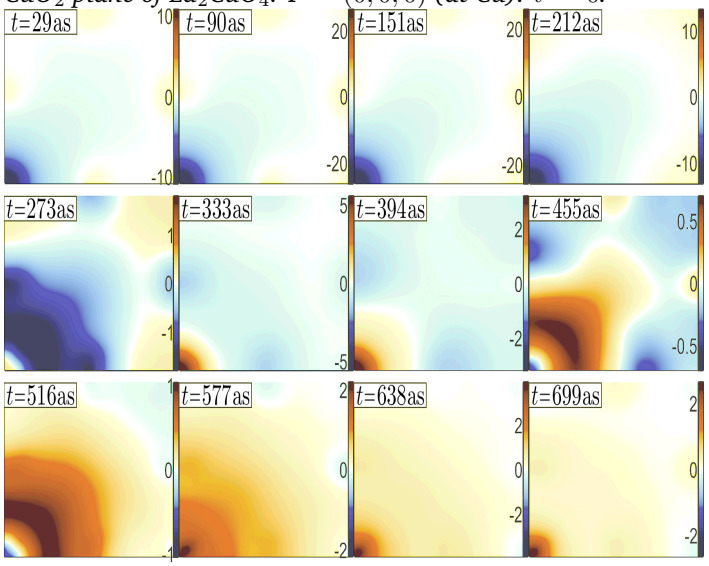

Figure 4.18: $U_3(\mathbf{r},\mathbf{r}';t)$ *(in* $\mathrm{eV}(152.26\,\mathrm{as})^{-1}$*) with* $\mathbf{r}$ *in the* CuO_2 *plane of* La_2CuO_4*.* $\mathbf{r}' = (0,0,0)$ *(at Cu).* $t' = 0$*.*

onds. The fact that W, U_1 and U_3 are so similar makes it more satisfactory to study the differences $W - U_1$ (Fig. 4.19), $U_1 - U_3$ (Fig. 4.20) and $W - U_3$ (Fig. 4.21). The metallic screening within RPA, $W - U_1$ (Fig. 4.19), does not decay within the given time interval (up to 699 attoseconds) as W and U_1 do separately, meaning that it plays a proportionally greater role after some time than directly after the perturbation was applied. This can be understood in terms of the $d_{x^2-y^2}$-symmetry which makes up a great proportion of this screening channel. This orbital does not have any overlap with the divergence caused by the perturbation at $\mathbf{r} = (0,0,0)$ and $t = 0$. The Cu s-orbitals however, have an overlap and should thus play a relatively greater role in the screening at short times.

While $W - U_1$ is not that localized at Cu, the Cu d-O p screening $U_1 - U_3$ (Fig. 4.20) appears to be so for all presented times. This relates to the previous discussion on the static differences $W - U_1$ and $U_1 - U_3$ (Fig. 4.10-4.11). The short-time form of $W - U_1$, $U_1 - U_3$ and $W - U_3$ (Fig. 4.19-4.21) very much resemble the corresponding static differences (Fig. 4.10-4.12). This could not be said about W, U_1 and U_3 separately because these include the bare interaction, v, which contains the effect of the instantaneous perturbation at $t = 0$. In the differences $W - U_1$, $U_1 - U_3$ and $W - U_3$ however, v is cancelled, making such an identification possible. The exact shape of the static differences can thus now be explained in terms of the screening phenomena occuring at different times. Since these differ-

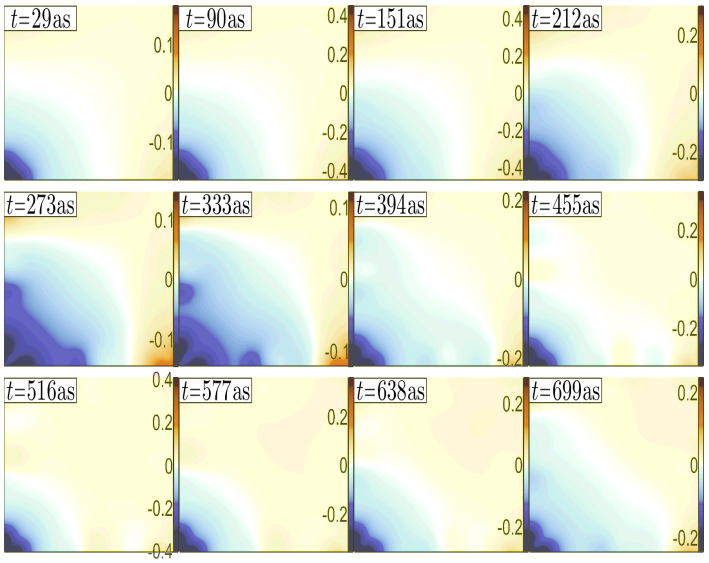

Figure 4.19: $(W - U_1)(\mathbf{r}, \mathbf{r}'; t)$ *(in* $\mathrm{eV}(152.26\,\mathrm{as})^{-1}$*) with* $\mathbf{r}$ *in the* CuO_2 *plane of* La_2CuO_4*.* $\mathbf{r}' = (0,0,0)$ *(at Cu).* $t' = 0$*.*

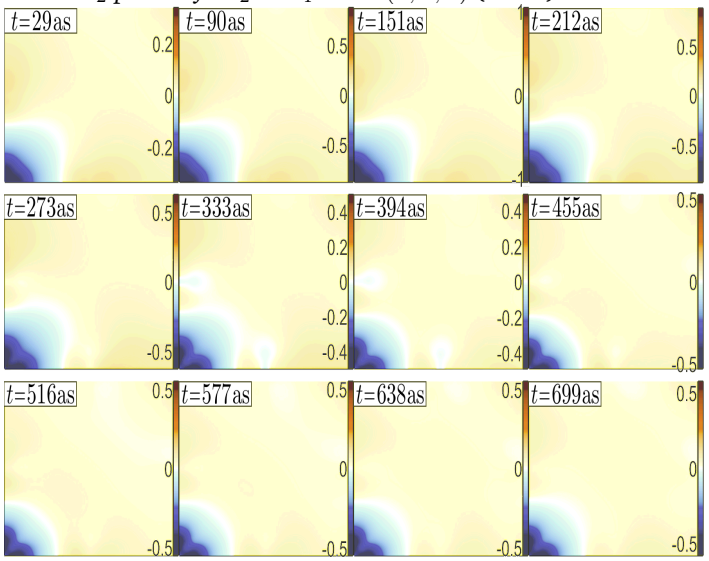

Figure 4.20: $(U_1 - U_3)(\mathbf{r}, \mathbf{r}'; t)$ *(in* $\mathrm{eV}(152.26\,\mathrm{as})^{-1}$*) with* $\mathbf{r}$ *in the* CuO_2 *plane of* La_2CuO_4*.* $\mathbf{r}' = (0,0,0)$ *(at Cu).* $t' = 0$*.*

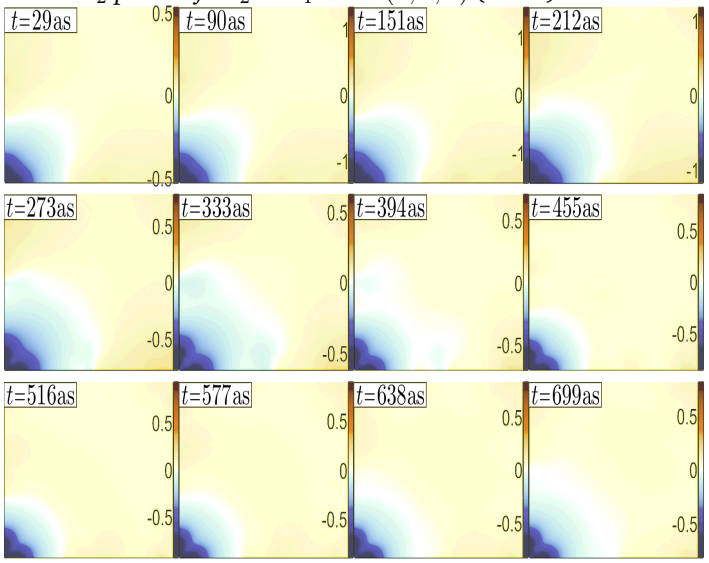

Figure 4.21: $(W - U_3)(\mathbf{r}, \mathbf{r}'; t)$ *(in* $\mathrm{eV}(152.26\,\mathrm{as})^{-1}$*) with* $\mathbf{r}$ *in the* CuO_2 *plane of* La_2CuO_4*.* $\mathbf{r}' = (0,0,0)$ *(at Cu).* $t' = 0$*.*

ences do not decay in the presented time-interval, this would require looking at longer times. However, the main channels seem to be taken into account, as seen by careful comparisons.

Perturbation at O

Similar results are here presented for W, U_1, U_3, $W-U_1$, U_1-U_3 and $W-U_3$ (Fig. 4.22-4.27) with $\mathbf{r}' = T_{\mathrm{L}}(0.5,0,0)$ (at O). Most has been said in the case of $\mathbf{r}'$ at Cu but attention should be paid on O p-Cu d hybridization, mainly in U_1-U_3 but also in $W-U_1$. $W-U_1$ eventually becomes localized at Cu despite the test charge at O. $W-U_1$ and U_1-U_3 are small compared to the case of $\mathbf{r}'$ at Cu, indicating that both metallic and Cu d-O p screening are located at Cu.

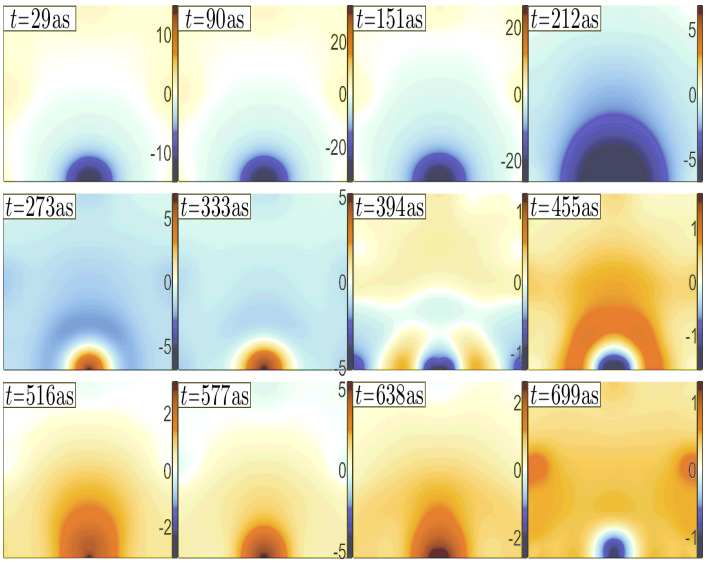

Figure 4.22: $W(\mathbf{r},\mathbf{r}';t)$ *(in* $\mathrm{eV}(152.26\,\mathrm{as})^{-1}$*) with* $\mathbf{r}$ *in the Cu-O$_2$ plane of La$_2$CuO$_4$.* $\mathbf{r}' = T_{\mathrm{L}}(0.5,0,0)$ *(at O).* $t' = 0$.

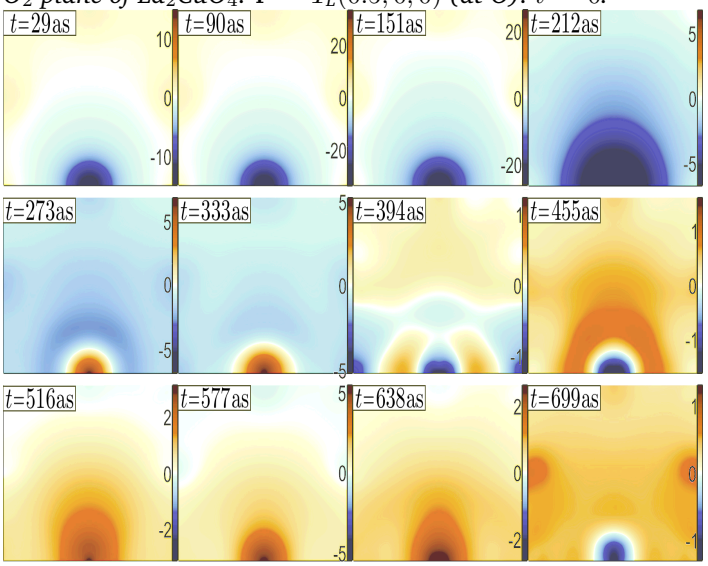

Figure 4.23: $U_1(\mathbf{r},\mathbf{r}';t)$ *(in* $\mathrm{eV}(152.26\,\mathrm{as})^{-1}$*) with* $\mathbf{r}$ *in the Cu-O$_2$ plane of La$_2$CuO$_4$.* $\mathbf{r}' = T_{\mathrm{L}}(0.5,0,0)$ *(at O).* $t' = 0$.

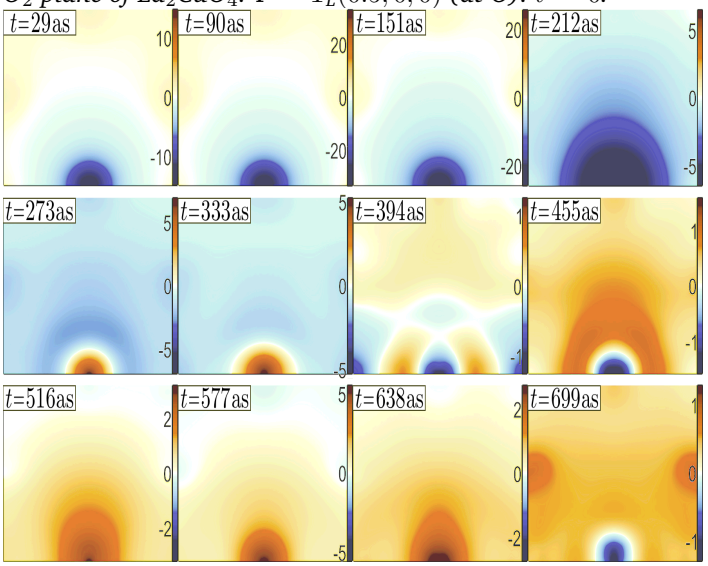

Figure 4.24: $U_3(\mathbf{r},\mathbf{r}';t)$ *(in* $\mathrm{eV}(152.26\,\mathrm{as})^{-1}$*) with* $\mathbf{r}$ *in the Cu-O$_2$ plane of La$_2$CuO$_4$.* $\mathbf{r}' = T_{\mathrm{L}}(0.5,0,0)$ *(at O).* $t' = 0$.

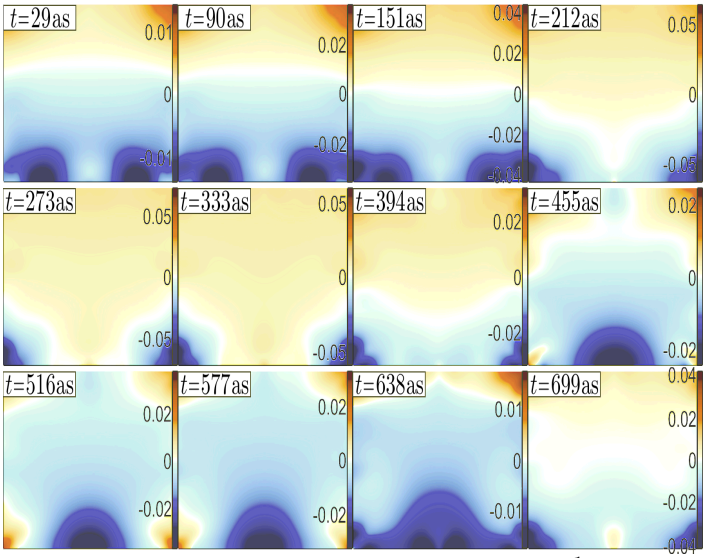

Figure 4.25: $(W - U_1)(\mathbf{r}, \mathbf{r}'; t)$ *(in* $\mathrm{eV}(152.26\,\mathrm{as})^{-1}$*) with* $\mathbf{r}$ *in the* CuO_2 *plane of* La_2CuO_4*.* $\mathbf{r}' = T_L(0.5, 0, 0)$ *(at O).* $t' = 0$*.*

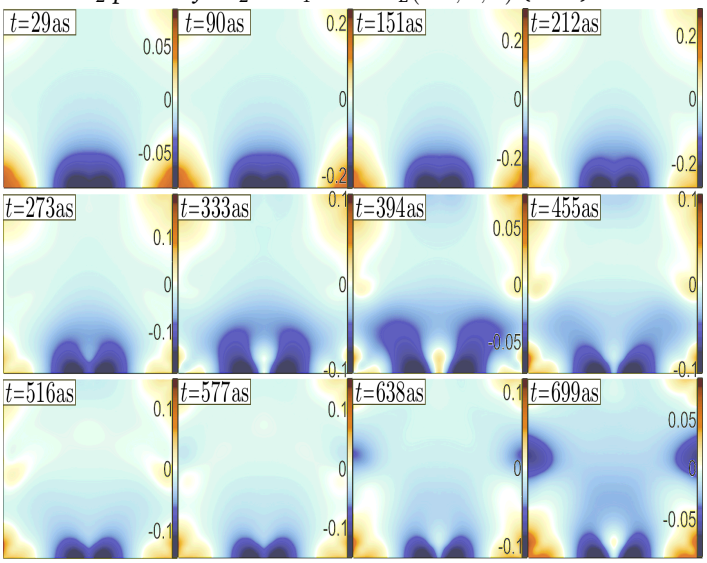

Figure 4.26: $(U_1 - U_3)(\mathbf{r}, \mathbf{r}'; t)$ *(in* $\mathrm{eV}(152.26\,\mathrm{as})^{-1}$*) with* $\mathbf{r}$ *in the* CuO_2 *plane of* La_2CuO_4*.* $\mathbf{r}' = T_L(0.5, 0, 0)$ *(at O).* $t' = 0$*.*

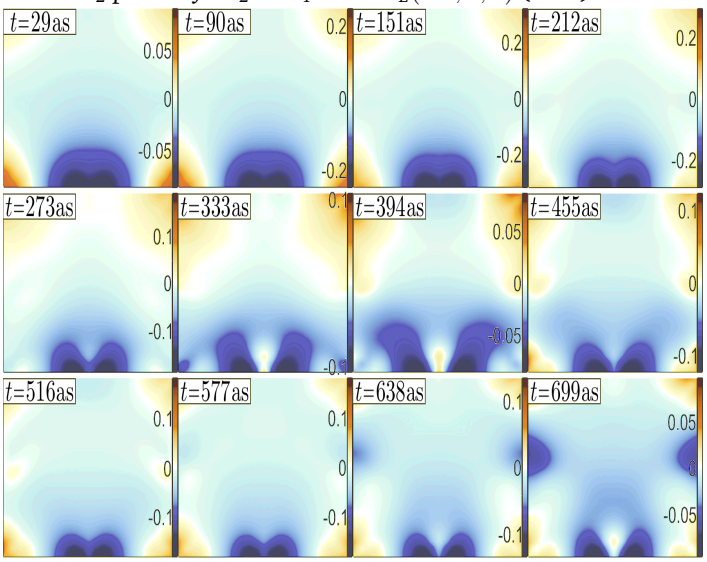

Figure 4.27: $(W - U_3)(\mathbf{r}, \mathbf{r}'; t)$ *(in* $\mathrm{eV}(152.26\,\mathrm{as})^{-1}$*) with* $\mathbf{r}$ *in the* CuO_2 *plane of* La_2CuO_4*.* $\mathbf{r}' = T_L(0.5, 0, 0)$ *(at O).* $t' = 0$*.*

Perturbation at M

While previously considering $\mathbf{r}'$ at different atomic sites (Cu and O), W, U_1, U_3, $W - U_1$, $U_1 - U_3$ and $W - U_3$ (Fig. 4.28-4.33) are here presented for $\mathbf{r}' = T_{\mathrm{L}}(0.5, 0.5, 0)$ (at M), far from any atom. Again, the results will not be discussed in detail, but note that along the lines of previous findings, W at short times (Fig. 4.28) is similar to the static W^c (Fig. 4.5). Also take notice on the Cu d-O p hybridization which is visible in $U_1 - U_3$ (Fig. 4.32).

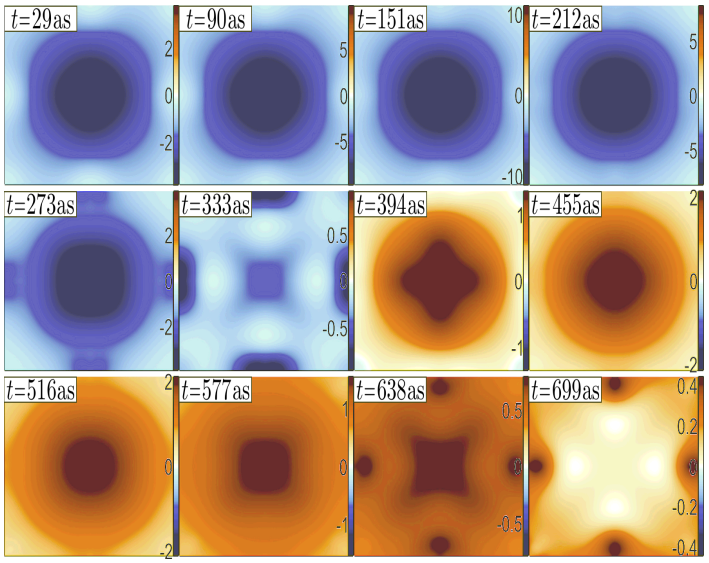

Figure 4.28: $W(\mathbf{r}, \mathbf{r}'; t)$ *(in* $\mathrm{eV}(152.26\,\mathrm{as})^{-1}$*) with* $\mathbf{r}$ *in the Cu-O₂ plane of* La_2CuO_4*.* $\mathbf{r}' = T_L(0.5, 0.5, 0)$ *(at M).* $t' = 0$*.*

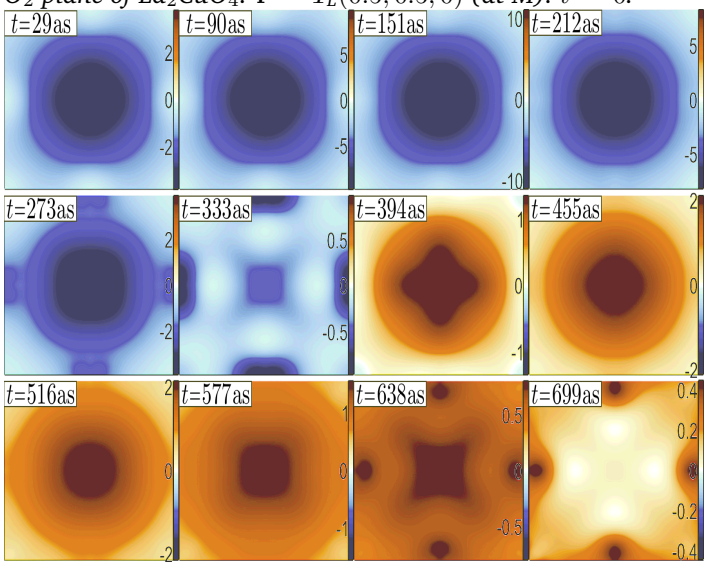

Figure 4.29: $U_1(\mathbf{r}, \mathbf{r}'; t)$ *(in* $\mathrm{eV}(152.26\,\mathrm{as})^{-1}$*) with* $\mathbf{r}$ *in the Cu-O₂ plane of* La_2CuO_4*.* $\mathbf{r}' = T_L(0.5, 0.5, 0)$ *(at M).* $t' = 0$*.*

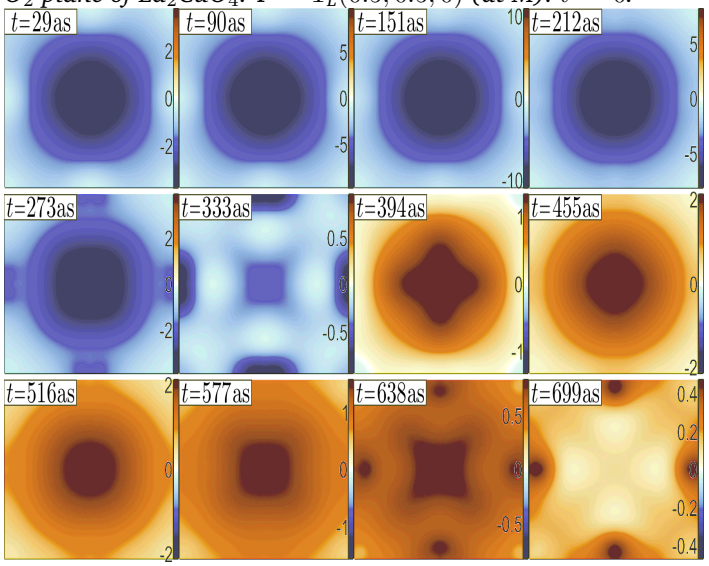

Figure 4.30: $U_3(\mathbf{r}, \mathbf{r}'; t)$ *(in* $\mathrm{eV}(152.26\,\mathrm{as})^{-1}$*) with* $\mathbf{r}$ *in the Cu-O₂ plane of* La_2CuO_4*.* $\mathbf{r}' = T_L(0.5, 0.5, 0)$ *(at M).* $t' = 0$*.*

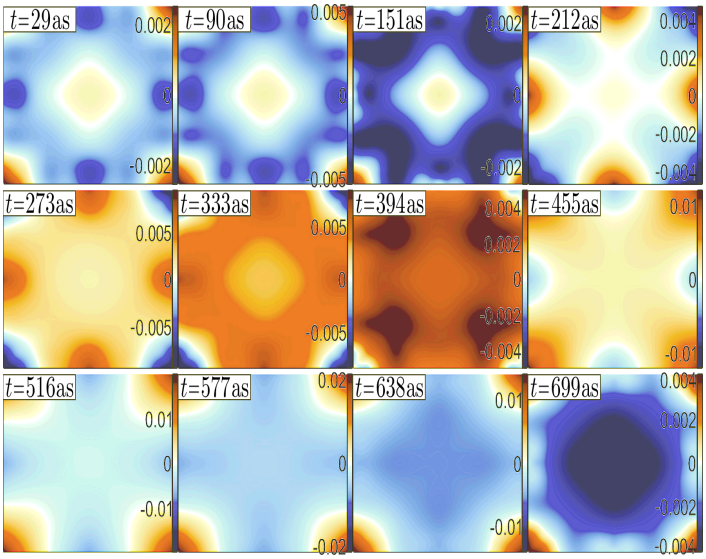

Figure 4.31: $(W - U_1)(\mathbf{r}, \mathbf{r}'; t)$ *(in* $\mathrm{eV}(152.26\,\mathrm{as})^{-1}$*) with* $\mathbf{r}$ *in the* CuO_2 *plane of* La_2CuO_4*.* $\mathbf{r}' = T_L(0.5, 0.5, 0)$ *(at M).* $t' = 0$*.*

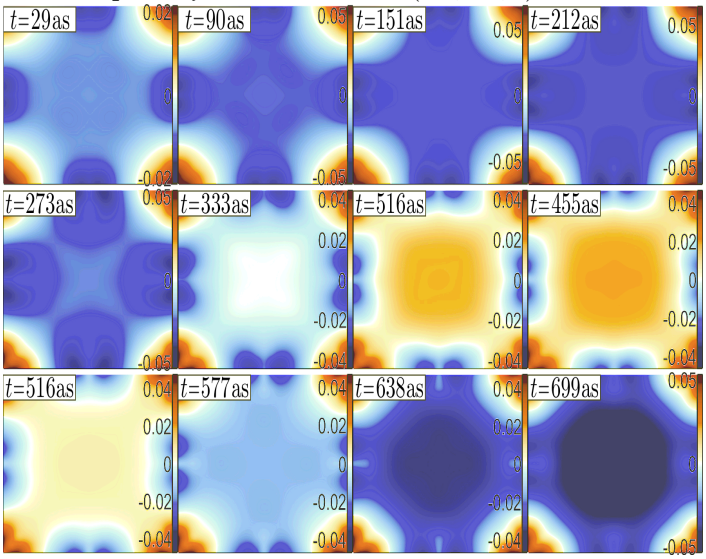

Figure 4.32: $(U_1 - U_3)(\mathbf{r}, \mathbf{r}'; t)$ *(in* $\mathrm{eV}(152.26\,\mathrm{as})^{-1}$*) with* $\mathbf{r}$ *in the* CuO_2 *plane of* La_2CuO_4*.* $\mathbf{r}' = T_L(0.5, 0.5, 0)$ *(at M).* $t' = 0$*.*

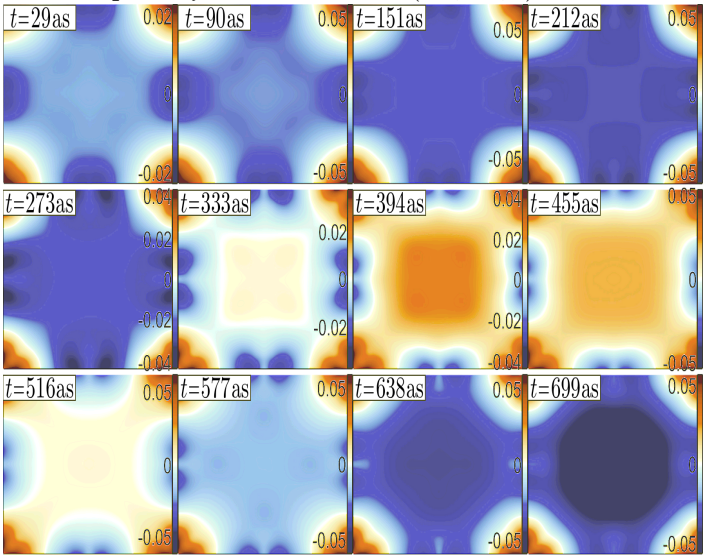

Figure 4.33: $(W - U_3)(\mathbf{r}, \mathbf{r}'; t)$ *(in* $\mathrm{eV}(152.26\,\mathrm{as})^{-1}$*) with* $\mathbf{r}$ *in the* CuO_2 *plane of* La_2CuO_4*.* $\mathbf{r}' = T_L(0.5, 0.5, 0)$ *(at M).* $t' = 0$*.*

Moving the Perturbation

In an attempt to summarize the results in space and time, U_1 is presented (Fig. 4.34) at chosen times (columns) for $\mathbf{r}'$ along the triangular path introduced earlier: $(0,0,0)$ (row 1), $(\frac{T_L}{4},0,0)$ (row 2), $(\frac{T_L}{2},0,0)$ (row 3), $(\frac{T_L}{2},\frac{T_L}{4},0)$ (row 4), $(\frac{T_L}{2},\frac{T_L}{2},0)$ (row 5) and $(\frac{T_L}{4},\frac{T_L}{4},0)$ (row 6). In this way, U_1 is resolved not only in $\mathbf{r}$ and t, but also in $\mathbf{r}'$ (though more roughly).

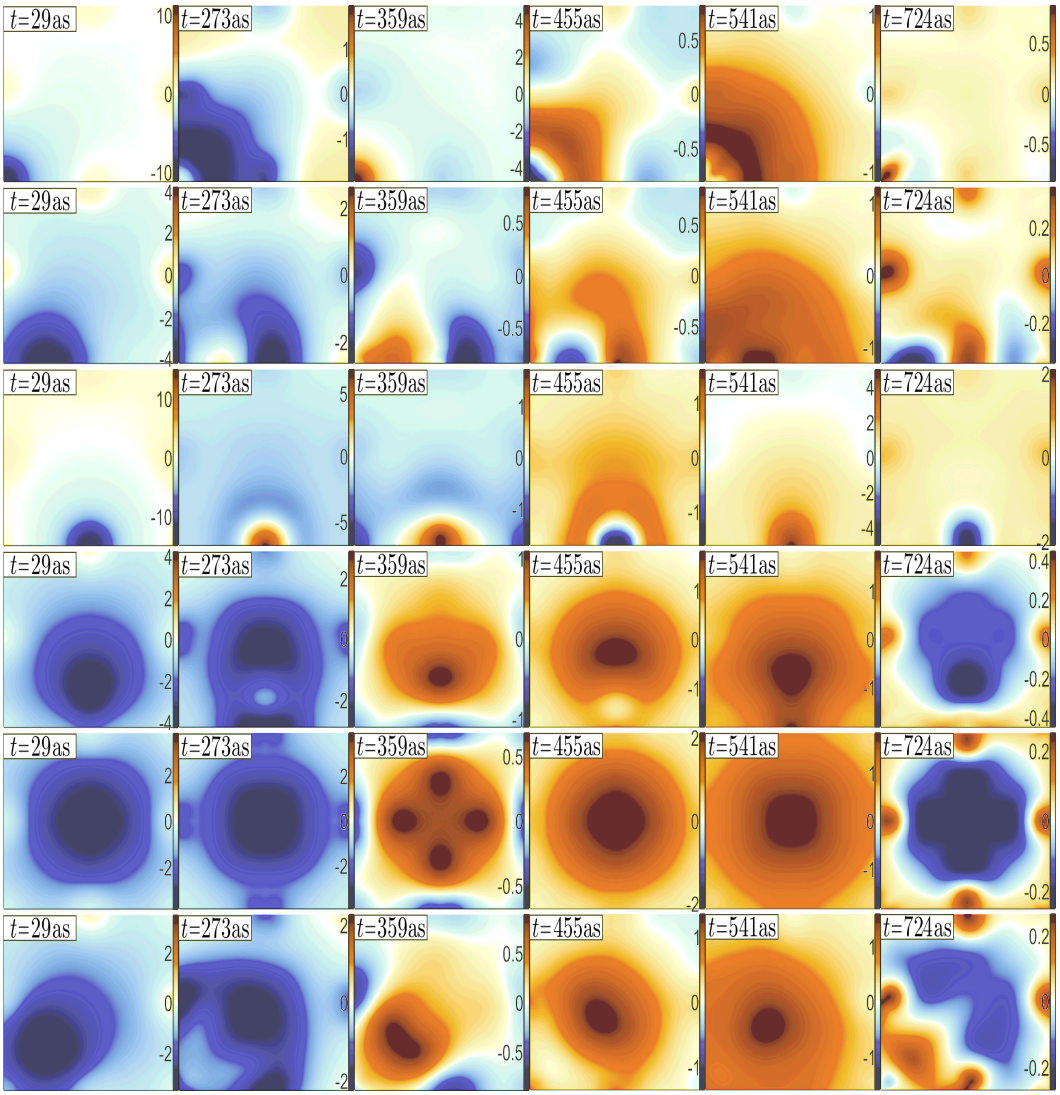

Figure 4.34: $U_1(\mathbf{r},\mathbf{r}';t)$ *(in* $\mathrm{eV}(152.26\,\mathrm{as})^{-1}$*) with* $\mathbf{r}$ *in the* CuO_2 *plane of* La_2CuO_4. $\mathbf{r}' = (0,0,0)$ *(row 1),* $T_L(0.25,0,0)$ *(row 2),* $T_L(0.5,0,0)$ *(row 3),* $T_L(0.5,0.25,0)$ *(row 4),* $T_L(0.5,0.5,0)$ *(row 5),* $T_L(0.25,0.25,0)$ *(row 6).* $t' = 0$.

Chapter 5

Summary and Conclusions

The main findings made in this study can be summarized as follows, keeping in mind that it is the real-part of each quantity that is actually referred to:

- The static W has been shown to have a clear V d_{xy}-character (V: Vanadium) in $SrVO_3$ (Fig. 4.6), in accordance with [26], and Cu $d_{x^2-y^2}$-character in La_2CuO_4 (Fig. 4.7). These symmetries are even more visible in $\delta\rho$ (Fig. 4.3-4.4) of these compounds.
- Large regions of negative static W have been found in La_2CuO_4 (Fig. 4.7) contrary to $SrVO_3$ (Fig. 4.6). Very similar regions have also been found for U_1 (Fig. 4.8) and U_3 (Fig. 4.9) in La_2CuO_4.
- The comparisons between the static U_1 and U_3 (Fig. 4.8-4.9, 4.11) in La_2CuO_4 have shown that the Cu d-O p screening is highly localized at Cu and also responsible for the negative on-site interaction at Cu. This screening channel (Fig. 4.11) has further been shown to change sign closer to the test charge than the static metallic screening ($W - U_1$) (Fig. 4.10), in accordance with the shorter hopping within the three-band model. The $9\,\mathrm{eV}$ excitation in the Cu d-O p screening has been witnessed dynamically as a decaying oscillation in time (Fig. 4.14).
- $\delta\rho$ (Fig. 4.15) has also been shown to yield oscillatory behavior in space and time (plasma oscillations) in La_2CuO_4, with a high complexity due to the crystal structure.
- The study of W (Fig. 4.16, 4.22, 4.28), U_1 (Fig. 4.17, 4.23, 4.29) and U_3 (Fig. 4.18, 4.24, 4.30) for La_2CuO_4 in space and time has shown that briefly after applying an instantaneous repulsive perturbation (electron) an attraction persists in the vicinity of this for a brief moment before the interaction starts to oscillate with increasing complexity. Since these oscillations decay, the time-integrated interaction ($\omega = 0$), which is usually refered to as static, is actually mainly influenced by the short-time interaction, with small complexity. The quick temporal decay means that the first oscillations may determine whether or not the static interaction is attractive or not. The comparisons of W, U_1 and U_3 in space and time have also provided insights into the dynamics of the orbitals responsible for the metallic screening ($W - U_1$) and Cu d-O p screening ($U_1 - U_3$).

Based on these findings a main concluding remark is: The regions of static attractive interaction (related to the short-time screening) in La_2CuO_4, or rather LDA-mimicked $La_{2-x}Sr_xCuO_4$, obtained for W, U_1, and U_3 for a variety of located test charges, contrary to $SrVO_3$, indicate that overscreening effects may be important in $La_{2-x}Sr_xCuO_4$. This is interesting, referring back to the aim of this work, since U_1 and U_3 model the effective interaction among the electrons that are generally believed to form Cooper pairs. Other pairing mechanisms are discussed more frequently in modern research, but there is no reason to exclude electronic overscreening, and the negative U_1 and U_3 open up a window for such further research.

Chapter 6

Future Directions

By comparing the static and dynamical effective interactions, U_1 and U_3, in space for different (multi-layer) cuprates, and also for pnictides (another class of high-T_C compounds, see [27]) the correlation between the strength of the attractive interaction and T_C can be investigated. Such a comparison could also provide clues to why some are hole- and some are electron-doped high-T_C superconductors.

Another direction to proceed is to construct an *ab initio* Hubbard-Holstein Hamiltonian (see [4]), with on-site interaction U, plasmon energy Ω and electron-plasmon coupling Λ (App. D:2), using the same frequency-dependent U as in this work. Within this model, the Eliashberg equations can be solved in a localized basis for the superconducting gap.

Appendix A

Fundamental Many-Body Theory

A:1 DFT and LDA

The many-electron Hamiltonian is generally written as

$$H = \sum_{n=1}^{N} \left[-\frac{1}{2}\nabla_n^2 + V(\mathbf{r}_n) \right] + \frac{1}{2} \sum_{n \neq m} v(|\mathbf{r}_n - \mathbf{r}_m|)$$

$v(|\mathbf{r}_n - \mathbf{r}_m|) = 1/|\mathbf{r}_n - \mathbf{r}_m|$ is the bare Coulomb interaction between two electrons at $\mathbf{r}_n$ and $\mathbf{r}_m$ and $V(\mathbf{r}_n) = -\sum_a \frac{Z_a}{|\mathbf{r}_n - \mathbf{R}_a|} + V_{\text{ext}}(\mathbf{r}_n)$ is the interaction between an electron at $\mathbf{r}_n$ and all nuclei and a sometimes present external potential. A fruitful simplification is density functional theory (DFT). The main parts of DFT are: 1) Hohenberg-Kohn theorem (original paper: [28]): The external potential and thereby the Hamiltonian, and hence also excited state properties, are by using the *variational principle* and proof by contradiction shown to be uniquely determined by the ground-state (GS) density (ensemble density in the degenerate case). 2) Kohn-Sham scheme: By writing the total energy as a functional of the GS density, utilizing the variational principle and conservation of charge, the interacting system can be replaced by a non-interacting (one-electron) system but with the true GS density which minimizes the energy. The Kohn-Sham equation reads [5] [29]

$$\left[-\frac{1}{2}\nabla^2 + V(\mathbf{r}) + V_{\text{H}}(\mathbf{r}) \right] \psi_n(\mathbf{r}) + V_{\text{xc}}(\mathbf{r})\psi_n(\mathbf{r}) = \varepsilon_n \psi_n(\mathbf{r}).$$

$V_{\text{H}}(\mathbf{r}) = \int d^3r' \rho(\mathbf{r}') v(|\mathbf{r} - \mathbf{r}'|)$ is the Hartree potential, $V_{\text{xc}}(\mathbf{r}) = \delta E_{\text{xc}}/\delta\rho(\mathbf{r})$ the universal (does not depend on external potential) local exchange (xc) potential (interaction between an electron and its xc hole, integrating to -1) and $\rho(\mathbf{r}) = \sum_{i=1}^{N} |\psi_i(\mathbf{r})|^2$. The *local density approximation* (LDA) corresponds to replacing the xc hole with that of the homogeneous electron gas, a fairly good approximation since: 1) The xc hole still integrates to -1, 2) The spherical average of the true xc hole happens to be very close to that of the electron gas, and only the spherical average enters the xc energy E_{xc}. Within LDA: [29]

$$E_{\text{xc}}^{\text{LDA}}[\rho] = \int d^3r \epsilon_{\text{xc}}(\rho)\rho(\mathbf{r}).$$

$\epsilon_{\text{xc}}(\rho)$ is the exchange-correlation energy per electron in a homogeneous electron gas of density ρ. The Kohn-Sham equation is solved iteratively since $\rho(\mathbf{r})$ enters $V_{\text{H}}(\mathbf{r})$ and $V_{\text{xc}}(\mathbf{r})$. DFT within LDA can be used (as in this thesis) when the strong correlations do not enter, only enter weakly, or are canceled in the studied quantities. If strong correlations are important for the particular study however, a many-body description is necessary. One then replaces V_{xc} by a non-local and energy-dependent self-energy Σ and solves the "quasiparticle equation" for the quasiparticle wavefunctions and energies $\{\Psi_n\}$ and $\{E_n\}$: [5]

$$\left[-\frac{1}{2}\nabla^2 + V(\mathbf{r}) + V_{\text{H}}(\mathbf{r}) \right] \Psi_n(\mathbf{r}) + \int d^3r' \Sigma(\mathbf{r}, \mathbf{r}'; E_n)\Psi_n(\mathbf{r}') = E_n \Psi_n(\mathbf{r}).$$

A:2 Σ and G

Σ enters more naturally in the Green function formalism. In the Heisenberg picture, for a N-particle system with ground state $|N\rangle$, the one-particle Green function reads [5]

$$G(x,x') = -i\langle N|\mathcal{T}[\hat{\psi}(x)\hat{\psi}^\dagger(x')]|N\rangle.$$

$\mathcal{T}$ is the time-ordering operator, $\hat{\psi}$ the field operator and $x = (\mathbf{r},t)$. For $t > t'$ G is the probability amplitude that an electron propagates from x to x' and for $t' > t$ a hole from x to x'. The equation of motion for G has a term with four field operators corresponding to a two-particle Green function $G^{(2)}$ whose equation involves $G^{(3)}$ etcetera. By defining the mass operator $M(x,x')$ by

$$\int d^4x_1 M(x,x_1)G(x_1,x') = -i\int dt_1 \int d^3r_1 v(|\mathbf{r}-\mathbf{r}_1|)\langle N|\mathcal{T}[\hat{\psi}^\dagger(\mathbf{r}_1,t_1)\hat{\psi}(\mathbf{r}_1,t_1)\hat{\psi}(\mathbf{r},t)\hat{\psi}^\dagger(\mathbf{r}',t')]|N\rangle$$

the hierarchy is broken and the equation for G becomes (with $\delta^{(4)}(x-x') = \delta^{(3)}(\mathbf{r}-\mathbf{r}')\delta(t-t')$)

$$\left[i\frac{\partial}{\partial t} - h_0(x)\right] G(x,x') - \int dx_1 M(x,x_1)G(x_1,x') = \delta^{(4)}(x-x')$$

where h_0 is the kinetic energy operator plus additional one-particle fields. Defining the self-energy as $\Sigma = M - V_{\mathrm{H}}$ and Fourier transforming yields

$$\left[\omega - h_0(\mathbf{r}) - V_{\mathrm{H}}(\mathbf{r})\right] G(\mathbf{r},\mathbf{r}';\omega) - \int d^3r_1 \Sigma(\mathbf{r},\mathbf{r}_1;\omega)G(\mathbf{r}_1,\mathbf{r}';\omega) = \delta^{(3)}(\mathbf{r}-\mathbf{r}').$$

The non-interaction Green function G_0 is solution for $\Sigma = 0$. On matrix form, $G_0 = (\omega - h_0 - V_{\mathrm{H}})^{-1}$, leading to the Dyson equation [5]

$$G = G_0 + G_0\Sigma G = (G_0^{-1} - \Sigma)^{-1}.$$

A:3 P, R and W

In terms of a probing field φ (total field $V = \varphi + V_{\mathrm{H}}$) the inverse dielectric function ϵ^{-1}, polarization function P and linear density response function R are defined as [3] [21]

$$\begin{aligned}
\epsilon^{-1}(x_1,x_2) &\equiv \frac{\delta V(x_1)}{\delta\varphi(x_2)} \\
P(x_1,x_2) &\equiv \frac{\delta\rho(x_1)}{\delta V(x_2)} \\
R(x_1,x_2) &\equiv \frac{\delta\rho(x_1)}{\delta\varphi(x_2)}.
\end{aligned}$$

The screened interaction W is further defined as $W(x_1,x_2) \equiv \int d^4x_3 \epsilon^{-1}(x_1,x_3)v(|\mathbf{r}_3-\mathbf{r}_2|)$. The chain rule then yields (on matrix form $W = v + vPW = v + vRv$)

$$\begin{aligned}
W(x_1,x_2) &= v(|\mathbf{r}_1-\mathbf{r}_2|) + \int dx_3 dx_4 v(|\mathbf{r}_1-\mathbf{r}_3|)P(x_3,x_4)W(x_4,x_2) \\
&= v(|\mathbf{r}_1-\mathbf{r}_2|) + \int dx_3 dx_4 v(|\mathbf{r}_1-\mathbf{r}_3|)R(x_3,x_4)v(|\mathbf{r}_4-\mathbf{r}_2|).
\end{aligned}$$

W can be obtained self-consistently using Hedin's equations, which schematically read [21]

$$\begin{aligned}
W &= v + vPW \\
P &= -iG\Gamma G \\
G &= G^0 + G^0\Sigma G \\
\Sigma &= iWG\Gamma \\
\Gamma &= 1 + (\delta\Sigma/\delta G)GG\Gamma
\end{aligned}$$

Γ is the vertex function, and $\Gamma - 1$ are called "vertex corrections". For a simple interpretation of W, choosing $x_2 = (\mathbf{0}, 0)$ implies that $W(x_1) = v(|\mathbf{r}_1|) + \delta V_{\mathrm{H}}(x_1)$ where

$$\delta V_{\mathrm{H}}(x_1) = \int dx_3 v(x_1 - x_3)\delta\rho(x_3) \quad , \quad \delta\rho(x_3) = \int d4R(x_3, x_4)v(x_4)$$

$\delta\rho$ is the induced electron density and $v(x_4)$ has been treated as a perturbation. Since based on the variational principle, the electrons rearrange themselves to minimize the total energy, resulting in screening. [3] Fourier transforming $W(x_1, x_2) = W(\mathbf{r}_1, \mathbf{r}_2; t_1 - t_2)$ yields $W(\mathbf{r}_1, \mathbf{r}_2; \omega)$, which is the more commonly used representation.

A:4 Quasiparticles

For infinite periodic crystals the KS eigenstates can be labeled by the wave vector $\mathbf{k}$ and the band index n as $\phi_{\mathbf{k}n}(r)$. Without interactions, the spectral function reads $A^0(\mathbf{r}, \mathbf{r}'; \omega) \equiv -(1/\pi)\mathrm{Im}G^0(\mathbf{r}, \mathbf{r}'; \omega)\mathrm{sgn}(\omega - \mu) = \sum_{\mathbf{k}n} \phi_{\mathbf{k}n}(\mathbf{r})\phi^*_{\mathbf{k}n}(\mathbf{r}')\delta(\omega - \varepsilon_{\mathbf{k}n})$, where the one-particle excitation energy $\varepsilon_{\mathbf{k}n}$ is relative to the chemical potential μ. The diagonal elements are

$$A^0_{\mathbf{k}n}(\omega) = \delta(\omega - \varepsilon_{\mathbf{k}n}).$$

With interactions the $N\pm1$-particle states $|\Psi_n(N\pm1)\rangle$ are no longer single Slater-determinants resulting in broadening and shifting of the peak, describing a *quasiparticle*. The width is proportional to the inverse of the life-time. Using $G = [G_0^{-1} - \Sigma]^{-1}$ and assuming a diagonal Σ yields $G_{\mathbf{k}n}(\omega) = [\omega - \varepsilon_{\mathbf{k}n} - \Sigma_{\mathbf{k}n}(\omega)]^{-1}$ and

$$A_{\mathbf{k}n}(\omega) = -\frac{1}{\pi}\frac{\text{Im } \Sigma_{\mathbf{k}n}(\omega)}{[\omega - \varepsilon_{\mathbf{k}n} - \text{Re } \Sigma_{\mathbf{k}n}(\omega)]^2 + [\text{Im } \Sigma_{\mathbf{k}n}(\omega)]^2}$$

peaked at the quasi-particle energy $E_{\mathbf{k}n} = \varepsilon_{\mathbf{k}n} + \text{Re } \Sigma_{\mathbf{k}n}(\omega)$ with a height given by the inverse of Im $\Sigma_{\mathbf{k}n}(E_{\mathbf{k}n})$. Thus, Re$\Sigma$ shifts the quasi-particle energy and ImΣ is inversely proportional to the life-time. Normalization requires $\int d\omega A_{\mathbf{k}n}(\omega) = 1$ and $\sum_{\mathbf{k}n} \int d\omega A_{\mathbf{k}n}(\omega) = N$. [21] [30]

Appendix B

RPA and GWA

The random-phase approximation (RPA) is an approximation for the linear density response function R. Within RPA the response of the true interacting system to φ is assumed to be the same as that of a non-interacting system to $V = \varphi + V_{\mathrm{H}}$. In other words

$$R^{\mathrm{RPA}}\delta\varphi = P^0(\delta\varphi + \delta V_{\mathrm{H}}).$$

Utilizing $\delta V_{\mathrm{H}} = v\delta\rho = vR\delta\varphi$ results in the RPA equation

$$R^{\mathrm{RPA}} = P^0 + P^0 v R^{\mathrm{RPA}}$$

where the non-interacting polarization P^0 replaces the interacting one in the usual equation $R = P + PvR$. [3] [21] This implies that $W = v + vP^0W = v + vR^{\mathrm{RPA}}v$, or more explicitly

$$\begin{aligned} W(\mathbf{r},\mathbf{r}';\omega) &= v(|\mathbf{r}-\mathbf{r}'|) + \int d^3r_1 d^3r_2 v(|\mathbf{r}-\mathbf{r}_1|)P^0(\mathbf{r}_1,\mathbf{r}_2;\omega)W(\mathbf{r}_2,\mathbf{r}';\omega) \\ &= v(|\mathbf{r}-\mathbf{r}'|) + \int d^3r_1 d^3r_2 v(|\mathbf{r}-\mathbf{r}_1|)R^{\mathrm{RPA}}(\mathbf{r}_1,\mathbf{r}_2;\omega)v(|\mathbf{r}_2-\mathbf{r}'|) \end{aligned}$$

where P^0 can be shown to be given by [3]

$$\begin{aligned} P^0(\mathbf{r},\mathbf{r}';\omega) = \sum_{\sigma} \sum_{\mathbf{k},\mathbf{k}'\in \mathrm{BZ}} \sum_{n}^{\mathrm{occ}} \sum_{n'}^{\mathrm{unocc}} & \phi^{\sigma *}_{\mathbf{k}n}(\mathbf{r})\phi^{\sigma}_{\mathbf{k}'n'}(\mathbf{r})\phi^{\sigma}_{\mathbf{k}n}(\mathbf{r}')\phi^{\sigma *}_{\mathbf{k}'n'}(\mathbf{r}') \\ & \times \left[\frac{1}{\omega + \varepsilon^{\sigma}_{\mathbf{k}n} - \varepsilon^{\sigma}_{\mathbf{k}'n'} + i0^+} - \frac{1}{\omega - \varepsilon^{\sigma}_{\mathbf{k}n} + \varepsilon^{\sigma}_{\mathbf{k}'n'} - i0^+}\right]. \end{aligned}$$

RPA is valid in the weak coupling regime, that is, when the kinetic energy of the electrons dominates the potential energy. Just as RPA is an approximation for R, the GW approximation (GWA) is an approximation for Σ, which is expanded to linear order in W, on matrix form:

$$\Sigma^{\mathrm{GWA}} = iGW.$$

Actually, both RPA and GWA can be achieved by neglecting variations of the self-energy in the vertex function Γ. Within RPA $\delta\Sigma/\delta\varphi$ is neglected and in GWA $\delta\Sigma/\delta V$ is neglected, both resulting in a simplified vertex $\Lambda = 1$. Still, the variation of V_H with respect to the probing field is taken into account, which is why RPA is sometimes called the time-dependent Hartree approximation (TDHA). [21]

Appendix C

The Hubbard Model

An interacting electron system has the Hamiltonian

$$\hat{H} = \sum_{ij} h^0_{ij} \hat{c}^\dagger_i \hat{c}_j + \frac{1}{2} \sum_{ijkl} v_{ij,kl} \hat{c}^\dagger_i \hat{c}^\dagger_k \hat{c}_l \hat{c}_j$$

$$h^0_{ij} = \int d^3r \phi^*_i(\mathbf{r}) h^0(\mathbf{r}) \phi_j(\mathbf{r})$$

$$v_{ij,kl} = \int d^3r d^3r' \phi^*_i(\mathbf{r}) \phi_j(\mathbf{r}) v(|\mathbf{r} - \mathbf{r}'|) \phi^*_k(\mathbf{r}') \phi_l(\mathbf{r}').$$

Here, $h^0(\mathbf{r}) = -\frac{1}{2}\nabla^2 + V_{\text{ext}}(\mathbf{r})$. $\{|\phi_i\rangle\}$ are typically Kohn-Sham wavefunctions where i denotes both orbital and spin. Hubbard argued that strongly correlated materials with partially filled narrow bands ($d_{x^2-y^2}$ band in La_2CuO_4) at the Fermi energi which dominate the macroscopic properties are well-described by the *Hubbard model* ($t_{ij} \equiv h^0_{ij}$ is called the "hopping") [3]

$$\hat{H} = \sum_{ij \subset \text{d}} t_{ij} \hat{c}^\dagger_i \hat{c}_j + \frac{1}{2} \sum_{ijkl \subset \text{d}}^{\text{on-site}} U_{ij,kl} \hat{c}^\dagger_i \hat{c}^\dagger_k \hat{c}_l \hat{c}_j.$$

where U is an effective interaction within the narrow bands (this low-energy subspace is labeled by "d" in the following), screened by the more extended electrons outside this subspace. With sufficient screening only on-site interactions are considered, so that i, j, k, l label the same site. The Hubbard model can be simplified if assuming only one band per site. This is the *one-band model* (spin is written explicitly)

$$\hat{H} = t \sum_{\sigma \langle ij \rangle \subset \text{d}} \hat{c}^\dagger_{i\sigma} \hat{c}_{j\sigma} + U \sum_{i \subset \text{d}} \hat{n}_{i\uparrow} \hat{n}_{i\downarrow}.$$

From this it is clear that U, the on-site repulsion, is the cost of double occupancy. $\langle ij \rangle$ limits hopping to the nearest neighbours, which is a common first approximation. This one-band model has only one independent parameter, U/t. [3] The first "hopping term" favours delocalization and the second "on-site repulsion term" favours localization, and the solution gets highly material dependent. When modeling the physics in the CuO_2 plane in cuprates the one-band d subspace has dominant Cu $d_{x^2-y^2}$-component. In a three-band model, also O p_x and O p_y are included. The interaction terms in such a three-band model read [11] [31]

$$U_{dd} \sum_{i \subset \text{d}} \hat{n}^d_{i\uparrow} \hat{n}^d_{i\downarrow} + U_{pp} \sum_{i \subset \text{d}} \hat{n}^p_{i\uparrow} \hat{n}^p_{i\downarrow} + U_{pd} \sum_{\sigma\sigma' \langle ij \rangle \subset \text{d}} \hat{n}^d_{i\sigma} \hat{n}^p_{i\sigma}$$

where U_{dd}, U_{pp} and U_{pd} are d-d, p-p and p-d interactions. $\hat{n}^d_{i\sigma}$ and $\hat{n}^p_{i\sigma}$ are the d and p number operators in orbital i with spin σ. Note that U is different in the one- and three-band model, due to different amount of screening from the high-energy subspace.

Appendix D
Superconductivity

The pairing between electrons will first be studied given an attractive interaction, then the interaction itself. Pairing is for *conventional* superconductors modeled by BCS theory, where electron-phonon coupling is the typical mediator. These have well-defined quasiparticles suitable in a Fermi liquid picture. For *unconventional* superconductors like the doped cuprates, this fails, and Eliashberg theory will be discussed, which replaces the non-local and instantaneous BCS picture by a local and dynamical (retarded) picture.

D:1 Conventional Superconductivity - BCS Theory

Within BCS theory the main equations are the *gap equation* and the *number equation*. Given a pairing interaction $V_{\mathbf{k}\mathbf{k}'}(\mathbf{q})$ and assuming singlet spin the Hamiltonian reads [32]

$$\hat{H} = \sum_{\mathbf{k}\sigma} \varepsilon_{\mathbf{k}} \hat{c}^\dagger_{\mathbf{k}\sigma} \hat{c}_{\mathbf{k}\sigma} + \sum_{\mathbf{q}} \sum_{\mathbf{k}\mathbf{k}'} V_{\mathbf{k}\mathbf{k}'}(\mathbf{q}) \hat{c}^\dagger_{\mathbf{k}'+\mathbf{q}/2,\uparrow} \hat{c}^\dagger_{-\mathbf{k}'+\mathbf{q}/2,\downarrow} \hat{c}_{-\mathbf{k}+\mathbf{q}/2,\downarrow} \hat{c}_{\mathbf{k}+\mathbf{q}/2,\uparrow}$$

where $V_{\mathbf{k}\mathbf{k}'}(\mathbf{q}) = -V_{\mathbf{k}-\mathbf{k}'}(\mathbf{q})$ due to symmetric spin. $\varepsilon_{\mathbf{k}}$ is the dispersion relative to the chemical potential μ. The energy at zero current and magnetic field is minimized if

$$\langle \hat{c}_{-\mathbf{k}+\mathbf{q}/2,\downarrow} \hat{c}_{\mathbf{k}+\mathbf{q}/2,\uparrow} \rangle \neq 0$$

only for $\mathbf{q} = \mathbf{0}$ (the pairing term), yielding

$$\hat{H} = \sum_{\mathbf{k}\sigma} \varepsilon_{\mathbf{k}} \hat{c}^\dagger_{\mathbf{k}\sigma} \hat{c}_{\mathbf{k}\sigma} - \sum_{\mathbf{k}} \left(\Delta^*_{\mathbf{k}} \hat{c}_{-\mathbf{k},\downarrow} \hat{c}_{\mathbf{k},\uparrow} + \Delta_{\mathbf{k}} \hat{c}^\dagger_{\mathbf{k},\uparrow} \hat{c}^\dagger_{-\mathbf{k},\downarrow} \right)$$

with $\Delta_{\mathbf{k}} = -\sum_{\mathbf{k}'} V_{\mathbf{k}\mathbf{k}'} \langle \hat{c}_{-\mathbf{k}',\downarrow} \hat{c}_{\mathbf{k}',\uparrow} \rangle$ and $V_{\mathbf{k}\mathbf{k}'} \equiv V_{\mathbf{k}\mathbf{k}'}(\mathbf{0})$. This describes particle pairs fluctuating from and into a reservoir. $\Delta_{\mathbf{k}}$ is the *gap function*. Diagonalization yields $\hat{H} = \sum_{\mathbf{k}\sigma} E_{\mathbf{k}} \hat{\gamma}^\dagger_{\mathbf{k},\sigma} \hat{\gamma}_{\mathbf{k},\sigma}$ where $\hat{\gamma}_{\mathbf{k},\sigma}$ annihilates a quasi-particle. $\hat{\gamma}_{\mathbf{k},\uparrow} = A_{\mathbf{k}} \hat{c}_{\mathbf{k},\uparrow} - B_{\mathbf{k}} \hat{c}^\dagger_{-\mathbf{k},\downarrow}$ and $\hat{\gamma}_{\mathbf{k},\downarrow} = A_{\mathbf{k}} \hat{c}_{\mathbf{k},\downarrow} + B_{\mathbf{k}} \hat{c}^\dagger_{-\mathbf{k},\uparrow}$. Then the *quasi-particle dispersion* $E_{\mathbf{k}}$ is given by (details in [32])

$$E_{\mathbf{k}} = \sqrt{\varepsilon^2_{\mathbf{k}} + |\Delta_{\mathbf{k}}|^2}$$

and $A^2_{\mathbf{k}} = 1/2(1 + \varepsilon_{\mathbf{k}}/E_{\mathbf{k}})$, $|B_{\mathbf{k}}|^2 = 1/2(1 - \varepsilon_{\mathbf{k}}/E_{\mathbf{k}})$. Given $\varepsilon_{\mathbf{k}}$ only $\Delta_{\mathbf{k}}$ is needed to determine $E_{\mathbf{k}}$. The zero temperature *gap equation* reads

$$\Delta_{\mathbf{k}} = -\frac{1}{2} \sum_{\mathbf{k}'} V_{\mathbf{k}\mathbf{k}'} \frac{\Delta_{\mathbf{k}'}}{\sqrt{|\varepsilon_{\mathbf{k}'}|^2 + |\Delta_{\mathbf{k}'}|^2}}$$

where $\langle \hat{\gamma}^\dagger_{\mathbf{k}\sigma} \hat{\gamma}_{\mathbf{k}\sigma} \rangle = 0$ for $T = 0$ is used. For $T > 0$: $\langle \hat{\gamma}^\dagger_{\mathbf{k}\sigma} \hat{\gamma}_{\mathbf{k}\sigma} \rangle = f_{\mathrm{T}}(E_{\mathbf{k}}) = (1 + \mathrm{e}^{E_{\mathbf{k}}/T})^{-1}$, with quasiparticle chemical potential $\mu_\gamma = 0$, [32] yielding the finite temperature *gap equation* and *number equation* (to conserve charge), also called the *BCS equations* [33] ($N(0)$ is the

normal density of states at μ)

$$\Delta_{\mathbf{k}} = -\frac{1}{2}\sum_{\mathbf{k}'} V_{\mathbf{k}\mathbf{k}'} \frac{\Delta_{\mathbf{k}'}}{\sqrt{|\varepsilon_{\mathbf{k}'}|^2 + |\Delta_{\mathbf{k}'}|^2}} \tanh\left(\frac{\sqrt{|\varepsilon_{\mathbf{k}'}|^2 + |\Delta_{\mathbf{k}'}|^2}}{2T}\right)$$

$$n = 1 - \frac{1}{N(0)}\sum_{\mathbf{k}'} \frac{\varepsilon_{\mathbf{k}}}{\sqrt{|\varepsilon_{\mathbf{k}'}|^2 + |\Delta_{\mathbf{k}'}|^2}} \tanh\left(\frac{\sqrt{|\varepsilon_{\mathbf{k}'}|^2 + |\Delta_{\mathbf{k}'}|^2}}{2T}\right).$$

These are solved iteratively for $\Delta_{\mathbf{k}}$ and μ. [33] T_C is also obtained from the gap equation. Since $E_{\mathbf{k}} \geq |\Delta_{\mathbf{k}}| \geq 0$ the BCS-ground state must be proportional to $\prod_{\mathbf{k}\sigma} \hat{\gamma}_{\mathbf{k}\sigma}|0\rangle$, where $|0\rangle$ is the bare vacuum. [32] It thus costs to break the Cooper pair $(\uparrow \mathbf{k}, \downarrow -\mathbf{k})$.

For electron-phonon coupling, semiclassicaly, one electron compresses the positive lattice, which due to its retarded response attracts another electron. The two electrons form a Cooper pair, with a typical size of 100-1000 nm. [34] Emission/absorbtion of virtual phonons is often modeled as $V_{\mathbf{k}\mathbf{k}'} = -V\theta(\omega_D - |\varepsilon_{\mathbf{k}}|)\theta(\omega_D - |\varepsilon_{\mathbf{k}'}|)$. For conventional superconductors, μ is very close to that of the normal state and the number equation is skipped. Assuming a constant density of states when $\varepsilon_{\mathbf{k}} \in [-\omega_D, \omega_D]$, close to T_C in the weak-coupling limit yields $T_C = 1.13\omega_D \mathrm{e}^{-1/N(0)V}$. A material-independent ratio turns out to be $2\Delta(T=0)/T_C \approx 3.53$, but fails for large pairing interactions V for which the quasi-particles are ill-defined. [33] Then, Eliashberg theory is a more rigorous framework.

D:2 Unconventional Superconductivity - Eliashberg Theory

Superconductors that cannot be described by a Hartree-Fock BCS-theory are *unconventional*. Eliashberg theory incorporates frequency-dependence (retardation) and is local, and can thus describe the overscreening effects. The cuprates require a strong-coupling picture, where $\omega_D \sim 0.1 \times E_F$ and ω_D is the characteristic frequency of the bosons, which may have both phononic and electronic origin. Due to the pairing among d-electrons they also require a gap function of d-wave symmetry. They further require a conduction occupation away from half-filling and a proper treatment of the conduction bandwidth. There are ways of writing the strong-coupling Eliashberg equations, [33] however the main physics is more easily explained in a weak-coupling limit $N(0)V\omega_D/E_F \ll 1$, using Migdal theory, where vertex corrections are ignored. The electron-boson interaction is summarized by the Dyson equations

$$G^{-1}(\mathbf{k}, i\omega_n) = G_0^{-1}(\mathbf{k}, i\omega_n) - \Sigma(\mathbf{k}, i\omega_n) \;\;,\;\; G_0(\mathbf{k}, i\omega_n) = (i\omega_n \mathbf{1} - \varepsilon_{\mathbf{k}}\sigma_3)^{-1}$$

$$D^{-1}(\mathbf{q}, i\nu_n) = D_0^{-1}(\mathbf{q}, i\nu_n) - \Pi(\mathbf{q}, i\nu_n) \;\;,\;\; D_0^{-1}(\mathbf{q}, i\nu_n) = (M(\omega^2(\mathbf{q}) + \nu_n^2))^{-1}$$

for the electron (G) and boson (D) Green functions. G, G^0 and Σ are 2×2 matrices. $\varepsilon_{\mathbf{k}}$ is the one-electron Bloch energy, M the boson effective mass and $\omega(\mathbf{q})$ the boson dispersion. $\sigma_3 = (1\ 0\ ;\ 0\ \text{-}1)$ is a Pauli matrix. In general, there are many bosonic modes, λ. The Matsubara frequencies $\omega_n = (2n+1)\pi T$ and $\nu_n = 2n\pi T$ enter through the Fourier expansions

$$G(\mathbf{k}, \tau) = -\langle \mathcal{T}(\hat{\psi}_{\mathbf{k}}(\tau)\hat{\psi}_{\mathbf{k}}^\dagger(0))\rangle = T\sum_{n=-\infty}^{\infty} \mathrm{e}^{-i\omega_n\tau} G(\mathbf{k}, i\omega_n)$$

$$D_\lambda(\mathbf{q}, \tau) = -\langle \mathcal{T}(\hat{\varphi}_{\mathbf{q}\lambda}(\tau)\hat{\varphi}_{\mathbf{q}\lambda}^\dagger(0))\rangle = T\sum_{n=-\infty}^{\infty} \mathrm{e}^{-i\nu_n\tau} D_\lambda(\mathbf{q}, i\nu_n)$$

where $\hat{\psi}_{\mathbf{k}} = (\hat{c}_{\mathbf{k}\uparrow}\ \hat{c}_{-\mathbf{k}\downarrow}^\dagger)^T$ is the electron spinor and $\hat{\varphi}_{\mathbf{q}\lambda} = \hat{b}_{\mathbf{q}\lambda} + \hat{b}_{-\mathbf{q}\lambda}^\dagger$ the boson field of mode λ. The average is within a grand canonical ensemble: $\langle \hat{O}\rangle = \mathrm{tr}(\mathrm{e}^{-\hat{H}/T}\hat{O})/\mathrm{tr}(\mathrm{e}^{-\hat{H}/T})$, requiring a Hamiltonian, which is that of an electron-boson and electron-electron interaction

[33]

$$\hat{H} = \sum_{\mathbf{k}} \varepsilon_{\mathbf{k}} \hat{\psi}^\dagger_{\mathbf{k}} \sigma_3 \hat{\psi}_{\mathbf{k}} + \sum_{\mathbf{q}\lambda} \Omega_{\mathbf{q}\lambda} \hat{b}^\dagger_{\mathbf{q}\lambda} \hat{b}_{\mathbf{q}\lambda} + \sum_{\mathbf{k}\mathbf{k}'\lambda} \Lambda_{\mathbf{k}\mathbf{k}'\lambda} (\hat{b}_{\mathbf{k}-\mathbf{k}'\lambda} + \hat{b}^\dagger_{-(\mathbf{k}-\mathbf{k}')\lambda}) \hat{\psi}^\dagger_{\mathbf{k}'} \sigma_3 \hat{\psi}_{\mathbf{k}}$$
$$+ \frac{1}{2} \sum_{\mathbf{k}\mathbf{k}'\mathbf{k}''\mathbf{k}'''} v_{\mathbf{k}''\mathbf{k}''';\mathbf{k}\mathbf{k}'} (\hat{\psi}^\dagger_{\mathbf{k}''} \sigma_3 \hat{\psi}_{\mathbf{k}}) (\hat{\psi}^\dagger_{\mathbf{k}'''} \sigma_3 \hat{\psi}_{\mathbf{k}'}).$$

$\Omega_{\mathbf{q}\lambda}$ is the bare boson energy, $\Lambda_{\mathbf{k}\mathbf{k}'\lambda}$ the electron-boson matrix elements and v the Coulomb potential. Using Migdal's approximation (ignoring vertex corrections) the electron self-energy is

$$\Sigma(\mathbf{k}, i\omega_n) = -T \sum_{\mathbf{k}'n'\lambda} \sigma_3 G(\mathbf{k}', i\omega_{n'}) \sigma_3 \left[|\Lambda_{\mathbf{k}\mathbf{k}'\lambda}|^2 D_\lambda(\mathbf{k}-\mathbf{k}', i\omega_n - i\omega_{n'}) + U(\mathbf{k}-\mathbf{k}') \right]$$
$$= i\omega_n [1 - Z(\mathbf{k}, i\omega_n)] \mathbf{1} + \chi(\mathbf{k}, i\omega_n)\sigma_3 + \phi(\mathbf{k}, i\omega_n)\sigma_1 + \bar{\phi}(\mathbf{k}, i\omega_n)\sigma_2.$$

U is the partially screened interaction, assumed to only depend on momentum transfer, and the second row is a Pauli expansion. $[G(\mathbf{k}, i\omega_n)]^{-1} = i\omega_n Z \mathbf{1} - (\varepsilon_{\mathbf{k}} + \chi)\sigma_3 - \phi\sigma_1 - \bar{\phi}\sigma_2$, so solving $\det G(\mathbf{k}, \omega) \equiv \Theta(\mathbf{k}, \omega) = 0$ yields $E_{\mathbf{k}}$ and thus $\Delta(\mathbf{k}, i\omega_n)$

$$E_{\mathbf{k}} = \sqrt{\left(\frac{\varepsilon_{\mathbf{k}} + \chi}{Z} \right)^2 + \frac{\phi^2 + \bar{\phi}^2}{Z^2}} \quad , \quad \Delta(\mathbf{k}, i\omega_n) = \frac{\phi - i\bar{\phi}}{Z}.$$

G is diagonal for $\phi = \bar{\phi} = 0$, the normal state. The renormalization Z and shift function χ are then determined by the normal state Σ. Non-zero ϕ or $\bar{\phi}$ has lower free energy and a superconducting state with a gap arises. The $\mathbf{1}$, σ_1, σ_2 and σ_3 terms in G result in one Eliashberg equation each when plugging into the Migdal's approximation for Σ, and the fifth is the number equation (where $\tilde{\phi}$ is either ϕ or $\bar{\phi}$)

$$i\omega_n [1 - Z(\mathbf{k}, i\omega_n)] = T \sum_{\mathbf{k}'n'\lambda} |\Lambda_{\mathbf{k}\mathbf{k}'\lambda}|^2 D_\lambda(\mathbf{k}-\mathbf{k}', i\omega_n - i\omega_{n'}) \frac{i\omega_{n'} Z(\mathbf{k}', i\omega_{n'})}{\Theta(\mathbf{k}', i\omega_{n'})}$$
$$\chi(\mathbf{k}, i\omega_n) = T \sum_{\mathbf{k}'n'\lambda} |\Lambda_{\mathbf{k}\mathbf{k}'\lambda}|^2 D_\lambda(\mathbf{k}-\mathbf{k}', i\omega_n - i\omega_{n'}) \frac{\chi(\mathbf{k}', i\omega_{n'}) + \varepsilon_{\mathbf{k}'}}{\Theta(\mathbf{k}', i\omega_{n'})}$$
$$\tilde{\phi}(\mathbf{k}, i\omega_n) = -T \sum_{\mathbf{k}n'\lambda} [|\Lambda_{\mathbf{k}\mathbf{k}'\lambda}|^2 D_\lambda(\mathbf{k}-\mathbf{k}', i\omega_n - i\omega_{n'}) - U(\mathbf{k}-\mathbf{k}')] \frac{\tilde{\phi}(\mathbf{k}', i\omega_{n'})}{\Theta(\mathbf{k}', i\omega_{n'})}$$
$$n = 1 - 2T \sum_{\mathbf{k}'n'} \frac{\chi(\mathbf{k}', i\omega_{n'}) + \varepsilon_{\mathbf{k}'}}{\Theta(\mathbf{k}', i\omega_{n'})}$$

where clearly U enters the gap equation through the ϕ and $\bar{\phi}$ equations. For large electron-boson couplings it has been shown, with a few simplifications, that there is no upper bound for T_C within Eliashberg theory, contrary to BCS theory. [33] From $E_{\mathbf{k}}$ it is clear that with $\Delta(\mathbf{k}, i\omega_n) \to \Delta(\mathbf{k})$, $Z(\mathbf{k}, i\omega_n) = 1$ and $\chi(\mathbf{k}, i\omega_n) = 0$ the BCS model is reproduced, which neglects retardation, strong-coupling and many-body effects.

Bibliography

[1] A. Damascelli, Z.-X. Shen and Z. Hussain. *Angle-resolved photoemission spectroscopy of the cuprate superconductors*, Rev. Mod. Phys. **75**, 473 (2003), p. 2, 7, 13-15, 45.

[2] G. S. Atwal and N. W. Ashcroft. *Polarization waves and superconducting instabilities in electron systems*, Phys. Rev. B **70**, 104513 (2004), p. 1-9.

[3] E. Pavarini, E. Koch, D. Vollhardt and A. Lichtenstein. The LDA+DMFT approach to strongly correlated materials. Reihe Modeling and Simulation, Vol. 1. Verlag des Forschungszentrum Jülich, 2011. Chapter 7. F. Aryaseiawan, T. Miyake and R. Sakuma, *The Constrained RPA Method for Calculating Hubbard U from First-Principles*, p. 2-13, 16-19.

[4] M. Casula, Ph. Werner, L. Vaugier, F. Aryasetiawan, A. J. Millis and S. Biermann. *Low-energy models for correlated materials: bandwidth renormalization from Coulombic screening*, Phys. Rev. Lett. **109**, 126408 (2012), p. 1-4.

[5] F. Aryasetiawan. *Correlation Effects in Solids from First Principles*. Tsukuba: Kyoto University (2000), p. 444, 446-447. [Online]. Available: `http://repository.kulib.kyoto-u.ac.jp/dspace/bitstream/2433/96909/1/KJ00004711290.pdf` [Accessed: 23- Jul- 2016].

[6] The Jülich FLAPW code family: SPEX-FLEUR. Jülich Forschungszentrum, Peter Grünberg Institut. [Online] Available: `http://www.flapw.de/pm/index.php?n=User-Documentation.SPEX-FLEUR` [Accessed: 27- Sep- 2016].

[7] The Jülich FLAPW code family: FLEUR. Jülich Forschungszentrum, Peter Grünberg Institut. [Online] Available: `http://www.flapw.de/pm/index.php?n=User-Documentation.FLEUR` [Accessed: 27- Sep- 2016].

[8] M. Springer and F. Aryasetiawan. *Frequency-dependent screened interaction in Ni within the random-phase approximation*, Phys. Rev. B **57**, 4364 (1998), p. 4.

[9] Crystal structure of La_2CuO_4 [Online]. Available: `https://commons.wikimedia.org/wiki/Category:Lanthanum_compounds#/media/File:La2CuO4_structure2.png` [Accessed: 16- Aug- 2016].

[10] L. Vaugier, H. Jiang and S. Biermann. *Hubbard U and Hund's Exchange J in Transition Metal Oxides: Screening vs. Localization Trends from Constrained Random Phase Approximation*, Phys. Rev. B **86**, 165105 (2012), p. 1.

[11] P. Werner, R. Sakuma, F. Nilsson and F. Aryasetiawan. *Dynamical screening in La_2CuO_4*, Phys. Rev. B **91**, 125142 (2015), p. 1-9.

[12] D. J. Scalapino. *The case for $d_{x^2-y^2}$ pairing in the cuprate superconductors*, Phys. Rep. 250 (1995), p. 334-341.

[13] A. Ino. (1999). *Photoemission Study of the High-Temperature Superconductor* $La_{2-x}Sr_xCuO_4$ (Thesis, University of Tokyo, Tokyo, Japan), p. 7-9. [Online]. Available: http://wyvern.phys.s.u-tokyo.ac.jp/f/Research/arch/Thesis_Ino.pdf [Accessed: 10- Apr 2016].

[14] J. O. Fjærestad. *Introduction to Green Functions and Many-Body Perturbation Theory*. Trondheim: Norwegian University of Science and Technology (2013), p. 14-18. Available: http://www.nt.ntnu.no/users/johnof/green-2013.pdf [Accessed: 27- Sep- 2016].

[15] O. K. Andersen, A. I. Liechtenstein, O. Jepsen and F. Paulsen. *LDA Energy Bands, Low-Energy Hamiltonians,* t', t'', $t_\perp(\mathbf{k})$ *and* $J_\perp$, J. Phys. Chem. Solids **56**, 1573 (1995), p. 1573-1591.

[16] F. Aryasetiawan, M. Imada, A. Georges, G. Kotliar, S. Biermann and A. I. Lichtenstein. *Frequency-Dependent Local Interactions and Low-Energy Effective Models from Electronic Structure Calculations*, Phys. Rev. B **70**, 195104 (2004); F. Aryasetiawan, J. M. Tomczak, T. Miyake and R. Sakuma. *Downfolded Self-Energy of Many-Electron Systems*, Phys. Rev. Lett. **102**, 176402 (2009), p. 1-2, 4.

[17] Customized Spex Documentation (Release 1.0) [Online]. Available: http://www.matfys.lth.se/staff/Rei.Sakuma/spex/cspex_doc.pdf [Accessed: 27- Sep- 2016].

[18] C. Friedrich, S. Blügel and A. Schindlmayr. *Efficient implementation of the GW approximation within the all-electron FLAPW method*, Phys. Rev. B **81**, 125102 (2010), p. 3-4.

[19] V. I. Anisimov. *Strong Coulomb Correlations in Electronic Structure Calculations: Beyond the Local Density Approximation*. Advances in Condensed Matter Science Vol. 1. (Gordon and Breach Science Publishers, 2000), p. 24-28.

[20] J. J. Sakurai and J. J. Napolitano. *Modern Quantum Mechanics - First Edition* (Addison Wesley Longman; Revised Edition, 1994), p. 398.

[21] F. Aryasetiawan. *Functional Derivative Technique*. Lund: Mathematical Physics, Lund University (no date), p. 7-11, 15-24, 26-30. [Online]. Available: http://www.teorfys.lu.se/staff/Claudio.Verdozzi/FunctionalD.pdf [Accessed: 23- Jul- 2016].

[22] Energy Unit Conversions. Halas Nanophotonics Group, Rice University. [Online] Available: http://halas.rice.edu/conversions [Accessed: 28- Sep- 2016].

[23] R. W. G. Wyckoff. *The Structure Of Crystals - Supplement for 1930-1934 to the second edition* (The Chemical Catalog Company Inc. 1935), p. 10.

[24] P. Villars. Material Phases Data System (MPDS), CH-6354 Vitznau, Switzerland (ed.) SpringerMaterials. *$SrVO_3$ Crystal Structure* [Online]. Available: http://materials.springer.com/isp/crystallographic/docs/sd_0553039 [Accessed: 1- Feb- 2016].

[25] A. K. Mahan, R. M. Martin and S. Satpathy. *Calculated effective Hamiltonian for* La_2CuO_4 *and solution in the impurity Anderson approximation*, Phys. Rev. B **38**, 6650 (1988).

[26] I. A. Nekrasov, G. Keller, D. E. Kondakov, A. V. Kozhevnikov, Th. Pruschke, K. Held, D. Vollhardt, V. I. Anisimov. *Explanation of the similarity of the experimental photoemission spectra of $SrVO_3$ and $CaVO_3$*, cond-mat/0312429 (2003), p. 2.

[27] M. R. Norman. *High-temperature superconductivity in the iron pnictides*, Phys. **1**, 21 (2008).

[28] P. Hohenberg and W. Kohn. *Inhomogeneous Electron Gas*, Phys. Rev. 136, B 864 (1964).

[29] K. Burke. *The ABC of DFT*. Irvine: Department of Chemistry, University of California (2007), p. 47-48, 65-66, 71-74. [Online]. Available: `http:/dft.uci.edu/doc/g1.pdf` [Accessed: 23- Jul- 2016].

[30] E. H. Hwang and S. Das Sarma. *Quasiparticle spectral function in doped graphene: Electron-electron interaction effects in ARPES*, Phys. Rev. B **77**, 081412(R) (2008), p. 1.

[31] W. Hanke, M.L. Kiesel, M. Aichhorn, S. Brehm and E. Arrigoni. *The 3-Band Hubbard-Model versus the 1-Band Model for the high-T_c Cuprates: Pairing Dynamics, Superconductivity and the Ground-State Phase Diagram*, Eur. Phys. J. Special Topics **188**, (2010). (Springer-Verlag; 2010), p. 15-32.

[32] C. L. Henley. Class Lecture, Topic: BCS Theory. Physics (7)636: Solid State II. Ithaca: Cornell Center for Materials Research, Cornell University (spring 2009), p. 755-762, 764. [Online]. Available: `http://www.lassp.cornell.edu/clh/Book-sample/7.3.pdf` [Accessed: 27- Jul- 2016].

[33] E. Pavarini, E. Koch and U. Schollwöck. Emergent Phenomena in Correlated Matter. Modeling and Simulation, Vol. 3. Verlag des Forschungszentrum Jülich, 2013. Chapter 13. G. A. C. Ummarino, *Eliashberg Theory*, p. 396-402, 407.

[34] H. Ibach and H. J. Lüth. *Solid-State Physics - Second Edition* (Springer; 2002), p. 250.